

Investigation on the Parameters Affecting the Accuracy of Material Property Determination of Aluminium Using Ring Hoop Tension Tests

Sophie Cook, Wishawin Lertnawapan, Demetri Gaffney, Daniel Lee, Tallulah Jackson-Coombs

Abstract

Global warming and the need to decrease carbon emissions has led to an increase in the development of hydrogen as an alternative fuel source, particularly within the aviation industry. The most established hydrogen storage method is through metal spun dome-shaped pressure vessels. Since failure within these components predominantly occurs in the hoop direction, characterising their hoop material properties is crucial to ensure structural integrity. There are currently limited methods to accurately determine these material properties. Ring hoop tension tests are the most established technique, but introduce additional parameters such as clearance and friction, which affect the accuracy of the measured material properties. This investigation utilised uniaxial tension tests to establish a baseline for comparison of material properties and also employed linear friction tests to quantify friction coefficients, identifying the optimal lubrication option available for use in the ring hoop tension tests. The lubrication that provided the lowest friction coefficient of 0.047 was the '2-layer reverse' that consisted of a combination of PTFE tape and silicone grease. A factorial style experiment was undertaken for the ring hoop tension test to systematically vary the parameters of friction and clearance and assess their impact. Finite element modelling was used to further explore the influence of these parameters. The finite element model aligned more closely with the experimental results for the yield strength rather than the ultimate tensile strength, with an error of as little as 0.25% for the yield strength. Both the experimental and finite element results showed that friction had a greater impact than clearance on the accuracy of the results.



Supervised by Dr. M J Peel

School of Electrical, Electronic, and Mechanical Engineering
University of Bristol
2025

Declaration

This project report is submitted towards an application for a degree at the University of Bristol. The report is based upon independent work by the candidates. All contributions from others have been acknowledged, and the supervisor is identified on the front page. The views expressed within the report are those of the authors and not of the University of Bristol.

We hereby assert our right to be identified as the authors of this report. We give permission to the University of Bristol Library to add this report to its stock and to make it available for consultation in the library, and for inter-library lending for use in another library. It may be copied in full or in part for any bona fide library or research worker on the understanding that users are made aware of their obligations under copyright legislation.

We hereby declare that the above statements are true.

The image shows five handwritten signatures arranged horizontally. From left to right: 1. A signature that appears to be 'Sophie Cook'. 2. A signature that appears to be 'Wishawin Lertnawapan'. 3. A signature that appears to be 'Demetri Gaffney'. 4. A signature that appears to be 'Daniel Lee'. 5. A signature that appears to be 'Tallulah Jackson-Coombs'.

© Sophie Cook, Wishawin Lertnawapan, Demetri Gaffney, Daniel Lee, Tallulah Jackson-Coombs
2025

Certification of ownership of the copyright in a dissertation presented as part of and in accordance with the requirements for the relevant degree at the University of Bristol.

This report is the property of the University of Bristol Library and may only be used with due regard to the authors. Bibliographical references may be noted but no part may be copied for use or quotation in any published work without prior permission of the authors. In addition, due acknowledgement for any use must be made.

Work Allocation

	SC	WL	DG	DL	TJC
Uniaxial Tension Tests					
Specimen Design				●	●
Experimental Preparation	●	○	●		
Practical	●		●		
Data Processing			●		
Linear Friction Test					
Experimental Preparation	●	●	●		
Practical	●	●	●		
Data Processing		●			
Ring Hoop Tension Test					
Specimen Design			●	●	●
Experimental Preparation	●	●	●		
Practical	●		●		
DIC Processing	●		●		
Data Processing		●			
Finite Element Analysis					
Analytical Model			●		
Uniaxial Tension Test Modelling				●	●
Ring Hoop Tension Test Modelling			●	●	●
Friction Investigation			●		○
Clearance Investigation			●		●

Majority = ●

Contribution = ●

Small Contribution = ○

We confirm that the information on this page accurately describes our individual contributions to the project.

Contents	4
1 Introduction (TJC)	5
2 Aim and Objectives (All)	6
3 Literature Review (SC)	6
3.1 Mechanical Testing of Tubular Components	6
3.2 Ring Hoop Tension Test Setup	8
4 Methodology	11
4.1 Uniaxial Tensile Testing (DG)	12
4.2 Linear Friction Testing (SC, WL)	13
4.3 Ring Hoop Tension Test (SC, WL)	16
4.4 FE Modelling (TJC, DL)	19
5 RHTT Analytical Stress Model (DG)	24
5.1 RHTT Analytical Stress Model Assumptions	24
5.2 RHTT Hoop Tensile Force Derivation	25
5.3 RHTT Dog-bone Cross-sectional Area Derivation	26
6 Results	27
6.1 Uniaxial Testing (DG)	27
6.2 Linear Friction Testing (SC, WL)	28
6.3 Ring Hoop Tension Test (SC, DG)	30
6.4 FE Modelling Results (DL, TJC, DG)	32
7 Discussion	38
7.1 Uniaxial Testing (DG)	38
7.2 Linear Friction Testing (SC, WL)	38
7.3 Ring Hoop Tension Test (SC, DG)	40
7.4 FE Modelling (DL, TJC, DG)	43
8 Critical Evaluation (All)	44
8.1 Limitations	45
8.2 Future work	46
9 Conclusion (All)	46

1 Introduction (TJC)

Alternative fuel sources are increasingly being explored for transportation and electricity generation due to the continued global push to reduce carbon emissions. A critical challenge faced with these new energy systems is the safe storage and handling of fuels. Many of these applications involve curved or cylindrical metal structures, such as pipes and pressure vessels, which are widely used in hydrogen storage, oil and gas transport, chemical processing and nuclear systems. The operation of these industries is highly regulated due to their use of safety critical infrastructure [1]. In these sectors, the safe design and manufacture of parts is crucial as failure can lead to leaks, explosions or contamination. Therefore, accurate mechanical testing of these curved components is essential in ensuring safe and reliable operation of these systems. Among the sectors exploring alternative fuels, the air transportation industry should be prioritised given that it accounted for 2.4% of global carbon emissions [2]. A promising alternative fuel source within the aviation industry is hydrogen, with companies allocating significant resources towards its research and development [3]. Hydrogen is commonly stored at high pressure in hemispherical dome-shaped pressure vessels made from aluminium [4]. Aluminium is the preferred material used within the aviation industry given its low density and high strength [5]. GKN Aerospace is at the forefront of the development of hydrogen-powered aircraft, which utilise these vessels for storage of hydrogen [6]. The failure of these vessels is a cause for major concern as hydrogen leakages can lead to explosions [7]. Therefore, the material properties of these vessels must be determined to ensure their capability to withstand high pressure and avoid failure.

Hollow dome shapes are manufactured from cold rolled sheets of aluminium, which are then hot metal spun to create domes and welded onto aluminium shells. This process alters the aluminium's material properties, so testing must be conducted to determine its new material properties. The assembly is currently tested using ultrasonic non-destructive testing to ensure there are no obvious flaws in the material. However, this test method does not quantify the material properties or account for any potential failure that may occur from hoop stresses. The dominating failure stress in these cylindrical pressure vessels is hoop stress [8]. This is due to failure by fracture being dominated by the hoop stress, while failure by yield is dominated by the equivalent stress, which includes both the hoop stresses and longitudinal stresses [8]. The pressure vessels can be assumed to be thin-walled, with the hoop stress twice the longitudinal stress and a negligible radial stress, which means that the failure by yield can be assumed to be dominated by hoop stress [8]. Therefore, the investigation of the material properties in the hoop direction is critical to ensure the safety and structural integrity of GKN's hydrogen storage vessels.

Uniaxial Tension Tests (UTT) could be used to determine material properties in the hoop direction. However, if conducted before metal spinning, the uniaxial test will not take into account the work hardening that the material undergoes in the process of metal spinning. Alternatively, if the test were to be performed after metal spinning, the material must first be flattened, which induces excess work hardening on the material. Therefore, UTTs will not be indicative of the true material properties of a metal spun component. Instead, to test hoop material properties in metal spun components such as the domes used in hydrogen pressure vessels, a Ring Hoop Tension Test (RHTT) should be used. This test method uses two hemispherical mandrels to pull a ring apart, allowing various material properties such as yield strength, Ultimate Tensile Strength (UTS), and ductility to be determined in the hoop direction. However, this test method introduces additional parameters which may influence the test results. These additional parameters include friction created by the contact between the mandrels and the ring specimen, and ring mandrel clearance due to the difficulty in manufacturing the ring specimens and mandrels with a tight fit. Currently, there are no standardised testing procedures to mitigate the effect of these variables in RHTTs. The aviation industry is highly regulated and, as hemispherical dome-shaped pressure vessels are commonly used, establishing standard test methods for material property determination of these metal spun components is essential. This report investigates the impact of friction and clearance on the accuracy of material property determination using a RHTT. The findings aim to assist GKN in developing a reliable testing approach for the metal spun components used in hydrogen pressure vessels for their aircraft.

2 Aim and Objectives (All)

The main aim of this study was to investigate which parameters have the greatest impact on the accuracy of RHTTs. The key material properties used to determine accuracy were yield strength, UTS, and the experimental ductility. The parameters investigated were friction and clearance between the ring specimen and mandrel. In order to achieve this aim, five objectives were identified as follows:

1. Critically review literature on the key parameters that influence the accuracy of ring hoop tension tests and to propose an optimal testing setup by utilising the current state of the art.
2. Perform standard tensile tests on samples with the same grain orientation as the ring samples, to provide a baseline for tensile properties for the chosen material.
3. Determine the estimated interface friction coefficients under varying lubrication conditions between tested aluminium and mandrel steel.
4. Determine the impact of ring-mandrel lubrication on the apparent material properties, using experimental and FE procedures.
5. Use experiments and FE modelling to evaluate the effect of the clearance between the mandrel and sample on the apparent material properties.

3 Literature Review (SC)

Pressurised cylindrical vessels used in the aviation and nuclear industries most frequently fail due to longitudinal cracks, which arise from hoop stresses induced by internal pressure loads. Since the stresses acting perpendicular to the cracks cause crack propagation and have the most significant impact, the mechanical properties in the hoop direction need to be determined [9]. The determination of the yield strength, UTS, and ductility of these tubular components is crucial for assessing the material's ability to withstand the stresses the component may encounter in service, and mitigate against the risk of failure. The mechanical testing procedures used to determine material properties in the hoop direction of tubular components are examined in the subsequent sections. The use of uniaxial tensile procedures that are adapted to test a tubular component was assessed, along with their associated limitations. Non-standard methods for hoop property evaluation were also considered, with current literature focusing on RHTTs as a developing technique. Accurate determination of material properties using this method requires specific attention to the test setup and procedure. Section 3.2 explores the literature on the recommendations aimed to minimise experimental limitations.

3.1 Mechanical Testing of Tubular Components

The processing of tubular components through methods such as rolling or extrusion induces work hardening in the material, leading to significant microstructural changes. These changes affect the material's grain size, and orientation, which in turn alters the macroscopic behaviour of the material, leading to the development of anisotropic material properties [10].

The application of conventional uniaxial testing procedures to tubular components introduces limitations, which result in inaccurate determination of the material properties in the hoop direction, as reviewed in Section 3.1.1. Various tests exist for quantifying material properties in the hoop direction, as discussed in 3.1.2, each with their own limitations [9][11]. There are currently no well-defined, standardised procedures for estimating these material properties, leading to variability in testing techniques and setups [12]. This inconsistency results in variations in material property estimations, depending on the methodology used. Therefore, there is a need for a standard procedure to accurately determine a material's hoop properties in order to ensure the structural integrity of safety-critical components.

3.1.1 Conventional Uniaxial Testing Techniques

Conventional Uniaxial Tension Tests (UTT), as outlined in ASTM E8, involve extracting and flattening a specimen from the longitudinal direction of the tube for testing [13]. However, flattening the specimen introduces a pre-strain into the material; therefore, the material properties derived from the tests do not

accurately reflect hoop direction behaviour [12]. Similarly, ASTM A370-22 outlines a similar method that uses a circumferential specimen, which assesses properties in the hoop direction [14]. This approach also requires the specimen to be flattened, and since it is a specimen from the circumferential direction, it incurs additional deformation compared to that of the ASTM E8 method. This affects the hoop material behaviour, altering its stress-strain curve and resulting in inaccurate property determination [10]. Another approach used is an axial tube tension test, which involves performing a tension test on a tube specimen with two gauges milled on opposite sides. This method avoids introducing a pre-strain into the material since no deformation occurs during the specimen's manufacture [15]. However, a significant limitation of the axial tube tension test is that tensile properties found from this test are in the longitudinal direction. Therefore, these material properties are not representative of the in-service loads these tubular components would be exposed to, which are in the hoop direction [15].

3.1.2 Hoop Testing Techniques

The current testing techniques for hoop property estimation can be split into two separate groups: qualitative and quantitative testing procedures.

Qualitative testing procedures provide insight into a specimen's loading capacity but do not directly determine specific material properties, where additional procedures, such as Finite Element Analysis (FEA), are required to quantify the material properties [16]. The potential testing procedures for metallic tubular components include the ring flattening/compression test (ISO 8492), drift expanding test (ISO 8493), flanging test (ISO 8494), ring expanding test (ISO 8495) and Ring Tensile Test (RTT) [16]. Chica et al. considered RTTs to be a qualitative testing procedure. It is defined in ISO 8496 as a test that uses two circular pins to expand the ring specimen. However, this method is only applicable to plastic pipes with an outside diameter exceeding 150 mm [16]. Other versions of the RTT, such as the split disc method and ring elongation test, introduce significant bending stresses into the specimen, leading to imprecise material property results [9]. These qualitative methods are appropriate for quality control or comparative assessments but do not yield precise numerical values for hoop mechanical properties.

Quantitative testing procedures provide direct measurements for one or more mechanical properties. These tests include the burst test, tube expansion test, tube end flaring, and Ring Hoop Tension Test (RHTT) [16]. However, as aforementioned, there are currently no standardised procedures for hoop property determination. The quantitative testing procedures are as follows:

- The burst test assesses the hoop properties through a pressure-controlled test that imposes a biaxial stress state similar to that experienced in hydrogen pressure vessels [12]. The test does not induce bending strain and is also independent of friction, but according to ASTM B811-13 the test specimen's length is required to be a minimum of ten times the average outer diameter, making this test impractical and infeasible since it would require pipe lengths of 1 m [17].
- The tube expansion test is similar to the burst test since it induces a biaxial stress state, but instead the tube is expanded using a mandrel or hydraulic pressure [18]. The testing equipment is relatively complex and requires a 'secure design conception', imposing limitations on testing capabilities [16].
- The tube end flaring test is an adaptation of the qualitative drift expanding technique, where in the tube flaring test a cone is advanced coaxially along the axis of the tube that causes the tube to expand [9]. Whilst this test is relatively simple, circumferential necking occurs due to the presence of friction, and biaxial stress fields are introduced into the specimen. Therefore, the failure limits obtained may not correspond to pure hoop tension [9][16].
- The RHTT is an adaptation of the RTT and instead uses mandrels to stretch the ring specimen without inducing significant bending in order to determine the material properties of a ring specimen [16], which can be machined from tubular components [12]. This testing technique is also applicable to materials other than plastic pipes, making it advantageous to the RTT. The increased contact between the mandrels and ring specimen in the RHTT induces greater friction, which has a negative impact on the deformation uniformity of the ring specimen that

can lead to inaccurate material property determination. The impact of friction can be mitigated through the use of lubrication [16][19]. Furthermore, scaling the mandrel diameter to the test specimen to reduce the clearance is crucial to avoid inducing bending stresses [16][17]. The effect of these parameters can be reduced through appropriate test set up and methodology. The RHTT technique requires a simple setup that does not induce a biaxial stress state and uses specimens that can be machined from a tubular component, making it a practical and advantageous approach compared to the other techniques discussed [12].

The RHTT has emerged as a leading technique for determining material properties in the hoop direction, since it provides a simple method that does not require extensive post-processing or additional analysis. The drawbacks of the RHTT include the introduction of friction and the potential for bending stresses when larger clearances are used. In literature, experimental studies and FEA have been conducted to assess the effects of friction and clearance on test accuracy. The mitigation of these effects is discussed in Section 3.2. A clear RHTT technique would provide a standard for hoop property estimation. This can be validated through FEA and UTTs with specimens made from the same sample and grain direction. A comprehensive comparison of these methods would provide a robust analysis of the key parameters affecting the RHTT, leading to clear setup recommendations to obtain accurate material tensile properties.

3.2 Ring Hoop Tension Test Setup

The application of RHTTs for hoop property estimation is an emerging and evolving field, with current literature focusing on different test configurations and their respective advantages. However, there remains no standardised procedure defining the most accurate and reliable RHTT setup and parameters. To accurately measure material properties, the RHTT setup must minimise bending stresses in the specimen and reduce the friction coefficient between the ring specimen and mandrels. There is a need to establish the most effective and accurate experimental RHTT methodology that incorporates the best practices from previous research to accurately determine material properties for safety-critical infrastructure.

3.2.1 Mandrel Configuration

Different configurations for the setup of RHTTs have been investigated through FE modelling and experimental testing to reduce the impact of stress non-uniformity, bending, and friction, which can lead to inaccurate determination of the material properties [19]. The introduction of bending stresses in the ring specimen results in stress non-uniformity, which can cause early failure and inaccurate material property measurements [19]. One critical parameter that affects the bending stresses in the ring specimen is the clearance, which is the difference in the diameter between the outer surface of the mandrel and the inner surface of the specimen. Due to the curved geometry of the specimen test shape, achieving uniform stress distribution in RHTTs is more challenging than in standard UTTs [15]. The friction between the mandrels and ring specimen significantly influences the apparent stress and deformation uniformity, which can produce inaccurate material properties [15]. Research has explored modifications to mandrel configuration, specimen geometry, and specimen positioning to minimise both clearance and frictional effects in the test setup. The mandrel configuration presents a trade-off between reducing bending stresses and increasing friction between the specimen and mandrel. Each configuration has an impact on the stress non-uniformity of the ring specimen since it affects the location and magnitude of the bending stresses, which can cause premature failure and inaccurate material property determination [19].

Wang et al. developed the RHTT procedure using two hemispherical mandrels with a specimen containing a single gauge positioned at 45° . This setup allowed for better preservation of the specimen's curvature, thereby reducing bending stresses in the specimen [15]. The bending and stress non-uniformity of the specimen is highly dependent on the number of dog-bone gauges on the specimen and their location, which is discussed in Section 3.2.3. One limitation of this configuration is increased friction between the mandrel and specimen due to a greater contact region. This could cause

underestimations in the ductility and overestimations in the strength measurements when the friction between the mandrel and ring is high [15]. Figure 1 shows the hemispherical mandrels with the case of a small and large clearance.

Arsene and Bai proposed a new mandrel design that consisted of a central insert in conjunction with two mandrels, as shown in Figure 1. This configuration aimed to restrict the bending stresses across the two-gauge regions, placed at 0° and 180° , in the specimen. Daum et al. further investigated this configuration for thin-walled isotropic steel tubes using FEA and validated it using experimental testing [20]. This data was compared to that from axial tube tension tests to assess the validity of this RHTT setup. The yield strength and UTS were obtained for this material; however, it was found that as the plastic displacements increased, the bending moments increased [15]. This caused premature necking and failure, resulting in an underestimation in the UTS. It was concluded that bending was not eliminated and stress non-uniformity persisted, making this setup the least favourable. Furthermore, friction was found to have a significant effect on the accuracy of the determination of deformation properties [20].

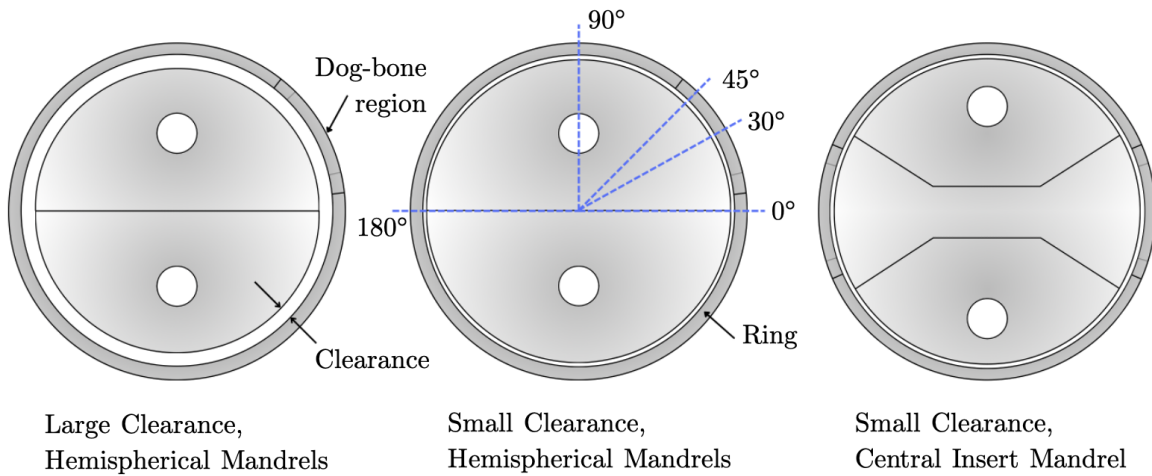


Figure 1: Diagram showcasing different mandrel designs.

Nagese et al. performed a comparative evaluation between the central insert configuration and hemispherical mandrels, concluding that the hemispherical mandrel configuration reduced bending, preserved uniaxial tension, and maintained stress uniformity better than that of the central insert [15]. Hansen et al. performed a comparison using FEA, with the specimen gauge being placed at 45° for the hemispherical mandrels, and two gauges being placed at 0° and 180° for the central insert mandrels. The difference in the number of gauges was accounted for by correcting the length to width ratio for the dog-bone gauge in the specimen. The study concluded that due to premature bending, the central insert mandrels underestimated the yield strength and UTS, and due to friction, the hemispherical setup overestimated the yield strength and UTS, compared to that of the material input. However, with mechanical correction factors or low friction, the hemispherical mandrel setup is recommended to provide ‘robust’ strength measurements [19]. Whilst this study provided an insight into the difference in bending moments between each mandrel configuration, it would be more beneficial to test each configuration consistently with two gauges placed at the same location. This would enable an understanding of the full effect of mandrel configurations on the bending stresses in the ring specimen.

3.2.2 Clearance

Beyond mandrel design, clearance between the mandrels and ring specimen significantly affects stress uniformity in the specimen, and therefore the accuracy of the material properties determined. The case of a larger clearance results in significant bending of the specimen as the ring is elongated into an oval shape. Conversely, with a smaller clearance and the mandrels matched closer to the specimen diameter, the bending effects are mitigated. However, this increased contact area between the mandrel and specimen increases friction [19]. Hansen et al. discovered the peak stress and strain in the ring

specimen tended to be located in the unsupported gap between the fixtures. Therefore, reducing the clearance would cause an increase in support for the ring specimen and consequently reduce the degree of the bending moment that is experienced. This led to the recommendation to minimise the clearance between the mandrels and ring specimen [19]. In practice, achieving precise mandrel to ring clearance is challenging due to machining tolerances. The tube diameter can vary along its axial length, which occurs in nuclear fuel cladding where thermal and irradiation-induced creep can alter the inner diameter dimensions along the tube [12][19]. Additionally, the clearance in test setups must be sufficient to accommodate lubricant. Therefore, the impact of clearance is a critical factor for evaluation, especially given that controlling it may not always be feasible. Whilst mandrel design investigations provide useful insight, existing studies suggest the hemispherical mandrels preserve stress uniformity the best. Therefore, further investigation should focus on the effect of clearance on hemispherical mandrels to clarify which levels may negatively impact material property determination.

3.2.3 Friction

Different researchers have suggested that the ring tensile load is a function of both friction and the orientation of the gauge [20]. Nagese et al. found that the gauge placed at the 90° position best reduced the effects of friction, whilst Dick et al. found this to be at 30° [15]. The orientation angles of the dog-bone gauge region are shown in Figure 1. Further research demonstrated that the frictional effect on the tensile load is lower when the gauge is positioned closer to the gap between the mandrels. Therefore, placing the dog-bone region on the ring specimen at a smaller angle helps to mitigate the effects of friction [19]. However, where friction can be significantly reduced through lubrication, such as PTFE tape and/or vacuum grease, the effect of gauge orientation on measured tensile strength becomes negligible [21].

A small variation in the level of friction can have a significant impact on the deformation uniformity in the dog bone region in the RHTT. High Friction Coefficients (FCs) between the mandrels and ring specimen can lead to stress non-uniformity, negatively affecting the accuracy of the material property determination. Dick et al. concluded that the FC needs to be kept below 0.1-0.15 in the case of hemispherical mandrels [12]. The effect of friction can be mitigated through increased lubrication. More recently, new mandrel designs have been developed to further reduce friction. These state-of-the-art designs incorporate radial needle bearings onto the mandrels, which decrease the friction by reducing the contact surface by ‘decreasing the resultant global contact frictional forces’ [22]. This experiment obtained a reduced FC of 0.011 for the radial needle bearing mandrels, from 0.111 for the hemispherical mandrels [22]. A simpler and widely adopted alternative utilises the application of Polytetrafluoroethylene (PTFE) tape and vacuum grease on the mandrels. This has been found to reduce the FCs from 0.3 (non-lubricated) to 0.02-0.04 [19]. Alternative lubricants can be used for testing in different environments, such as high temperature where a graphite-based lubricant would be required. However, for tests in standard conditions the use of PTFE and vacuum grease has been proven to provide an effective method for friction reduction, ensuring reliable material property determination.

3.2.4 Specimen Geometry

The geometry of the RHTT specimen varies based on the size of the dog-bone gauge and the number of gauges, ranging from none to two. The central insert mandrels make use of two gauges on opposite sides of the insert, as shown in Figure 1. In the case of a RHTT utilising hemispherical mandrels, one gauge region is commonly used [19]. The length to width ratio (l:w) of the machined dog-bone gauge is a critical parameter in ensuring strain uniformity at larger displacements whilst maintaining a uniaxial stress state [15]. The variation of gauge l:w ratios includes: 1:1, 1.5:1, 2:1, and 4:1. A higher gauge l:w, such as 4:1, enhances the preservation of uniaxial tension but can lead to a reduction in strain uniformity at larger displacements due to geometric limitations [15][19]. Lower ratios result in a higher stress concentration, which accelerates plastic deformation and causes early failure. These ratios have been utilised to introduce stress biaxiality into samples in order to replicate different failure modes and produce accident scenarios [19]. The ASTM E8 standard recommends a 4:1 l:w ratio for conventional

tensile testing, which when applied to a RHTT delays necking by promoting uniform strain along the gauge length [21].

3.2.5 RHTT Material Property Determination

Experimental studies have used uniaxial or axial tube tension tests using samples manufactured from the same tube as the ring specimens to assess and compare the accuracy of material property determination in the hoop direction [15]. FEA has been extensively utilised to analyse different test configurations and parameters, and to determine correction factors for more accurate property estimation. Analytical models have also been used to explore the effects of internal force distribution and friction between the mandrels and ring specimen [12]. FEA techniques can provide an advantage over experimental testing, given the correct resources and expertise, since they are more efficient. This makes FE modelling an effective method to evaluate experimental parameters before undertaking the experimental procedures. Dick et al. investigated the uniformity of the hoop stresses in the gauge region for the RHTT setup through the use of FE modelling. It was determined that the magnitude of the contact pressure between the ring and hemispherical mandrels, and the magnitude of the contact induced radial and axial stresses were comparable to those induced in burst test experiments. This validated the use of RHTTs for assessing hoop material properties for the case of low friction [12]. Kamerman et al. investigated the experimental RHTT setup using FEA, where it was noted that with the RHTT the engineering stress values can be reliably determined with knowledge of the applied load and the cross-sectional area of the test sample's gauge region. However, engineering strain values may not be reliably determined from just the mandrel displacement and gauge length [15]. Additionally, since it is difficult to achieve a uniaxial stress-strain state, it can be complicated to achieve a measurement for ductility with low strain rates or particularly brittle materials [23]. This means that the RHTT provides suitable evaluations for the yield strength and the UTS, but may only provide an indication of ductility [15]. Nagese et al. also identified that the RHTT was inadequate for producing Young's modulus results; this is due to the initial load displacement slope being too shallow, a conclusion that was further supported by Hansen et al. [19]. Nagese et al. concluded the shallow slope was due to bending induced plastic deformations occurring in the initial linear elastic region of the load displacement slope, whereas Hansen et al. attributed the shallow slope to compliance [1][19].

Research on RHTT has explored various fixture designs, specimen geometries, and RHTT parameters. The lack of standardisation has led to discrepancies in test parameters, which make it complicated to compare results across studies. Whilst recent work has delved into developing correction factors and innovative mandrel designs, these approaches may not be as impactful as establishing clear guidelines for key parameters such as the FC and clearance. Accurate material property determination for RHTTs would be conducted under optimal conditions with appropriate lubrication and therefore excessive focus on novel mandrel designs that reduce the FC may be unnecessary. Instead, this investigation proposes a systematic evaluation of fundamental test parameters. Previous studies have rarely assessed the relative importance of different test parameters in influencing material property determination. Additionally, current research draws conclusions or applies comparisons from experiments that can be inconsistent or use a limited number of ring specimens [12]. Therefore, a factorial experiment that systematically evaluates each key parameter, specifically the friction and clearance level, aims to provide a robust analysis to minimise variability seen in previous studies.

4 Methodology

This investigation will integrate the current best practices from previous literature to provide a comprehensive analysis on the mechanical factors affecting the RHTT. FE modelling and uniaxial tension tests will be utilised to validate RHTTs. The uniaxial data will be used in comparison with the RHTT and as a dataset for FE model material property definition. FE modelling will be used to assess the effects of key parameters on the accuracy of material determination using RHTTs. This investigation aims to provide a clear methodology that can be utilised by GKN Aerospace to evaluate the yield strength, UTS, and indications of the ductility for the metal spun components used in hydrogen pressure vessels.

4.1 Uniaxial Tensile Testing (DG)

The UTT results served as a baseline comparison to the RHTT results. To ensure equivalent specimens between the tests, the uniaxial specimens were machined from the same extruded aluminium 6082 T6 cylinder as the ring specimens. The gauge regions were orientated in the same grain direction as seen in Figure 2, to ensure comparable material properties. However, it was possible that the grain structure in the centre of the cylinder was marginally different from the grain structure at the outside of the cylinder due to extrusion strain.

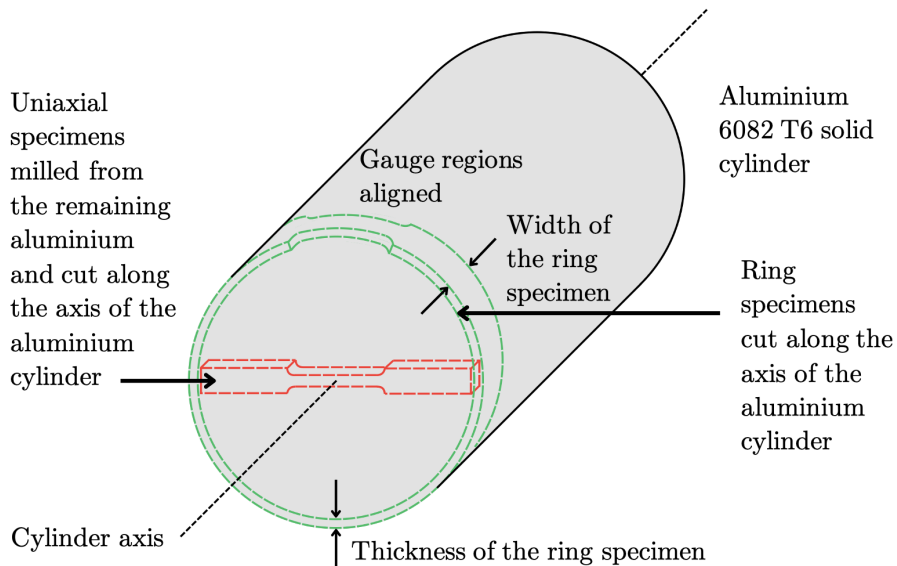


Figure 2: Diagram of the solid cylinder from which the uniaxial and ring specimens were machined.

The uniaxial specimens were designed according to the dimensions for a subsize specimen specified in ASTM E8 standards [24] as seen in Figure 3.

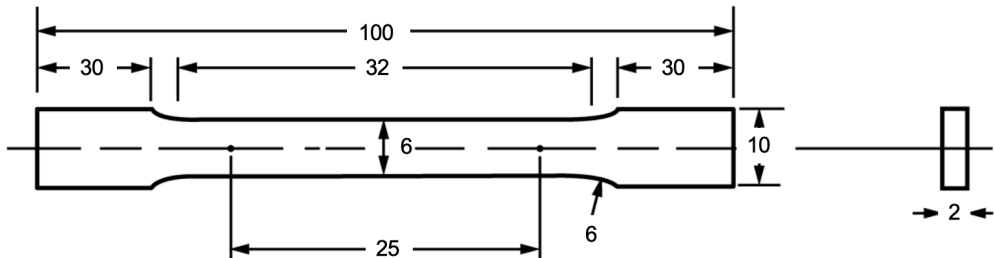


Figure 3: Engineering drawing of the uniaxial tensile specimen, detailing its dimensions in mm [24].

The UTTs were carried out using an INSTRON 1341 25 kN hydraulic testing machine and an INSTRON 8000 series data logger to measure the applied force. The lower actuator was assigned a displacement rate based on Section 7.6.4.2 of the ASTM E8 standard for tensile test methods of metallic materials [24], which specified a strain rate of 0.015/min for tensile property determination. The 32 mm length of the reduced parallel section from Figure 3 corresponds to a displacement rate of 0.48 mm/min.

Instead of using the INSTRON's actuator-based measurement, the displacement was measured by an Imetrum video extensometer. This was because the actuator would account for both the 'slipping' of the specimen between the grips and the change in length of the dog-bone region. The video extensometer only accounted for the change in length of the dog-bone region and was non-contacting, which meant that it did not influence the specimen strain.

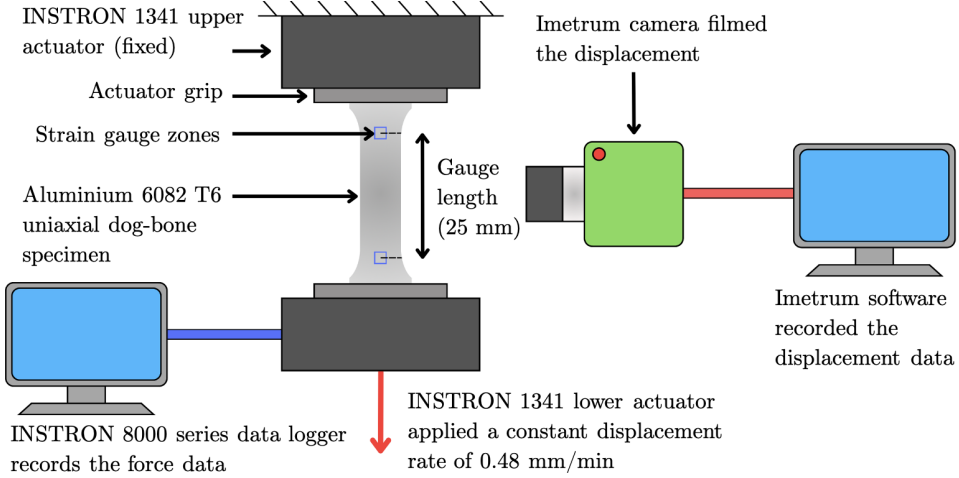


Figure 4: Diagram of the uniaxial test setup.

The uniaxial specimens were placed in the actuator grips in line with the axis of the applied tensile force, ensuring a uniform stress distribution. The video extensometer was calibrated by measuring the distance between two points on a ruler set against the surface of the specimen. This ensured accurate displacement measurements at the specimen's surface taken by the Imetrum camera. On the Imetrum software, a 25 mm extensometer and two gauge zones centred on the ends of the extensometer were digitally drawn on the specimen.

Data Processing

The stress-strain curves, shown in Sections 6.1 and 6.3.1, were a result of calculating the engineering stress from the force recorded by the INSTRON, and the strain from the displacement recorded by the Imetrum camera. The yield strength, UTS and ductility were calculated from the engineering stress-strain curves. The yield strength was defined as the stress at the intersection between the engineering stress-strain curve and the 0.2% strain offset line (gradient of the Young's modulus). The UTS was defined as the maximum value of engineering stress throughout a test. The ductility was defined as the value of strain immediately before failure. However, the FE model required the input of true plastic data, as detailed in Section 4.4.2. This is more representative of the actual stress and strain experienced by the specimens, as it considers the instantaneous stress-strain due to the changing length and cross-sectional area throughout a test.

4.2 Linear Friction Testing (SC, WL)

The Friction Coefficients (FCs) between the ring specimen and mandrels were quantified to enable the evaluation of different lubrication options. The lubrication option used in the RHTTs was dictated based on the option with the lowest average and most consistent FC.

4.2.1 Experimental (SC)

The FC between the mandrel and ring specimen was a key factor being investigated in the RHTTs. A Linear Friction Test (LFT) was used to quantify the FC between the Aluminium 6082 T6 (Al) ring specimen and the EN24T steel mandrels for use in the RHTT and FE model. The lubricants that were applicable for metals and therefore evaluated for the test were silicone grease and PTFE tape, with five lubrication options: Al-Dry-Steel (dry), Al-Grease-Steel (Grease), Al-PTFE-Steel (PTFE), Al-PTFE-Grease-Steel (2-layer), Al-Grease-PTFE-Steel (2-layer reverse), as shown in Figure 5. Each lubrication option was tested with five repeats. The lubrication option with the lowest average and most consistent FC was selected for use in the RHTT. To ensure consistency between the LFT and RHTT scenarios, the test was undertaken in the Coulomb friction regime. The steel samples had a milled finish, similar to that of the mandrels, and the aluminium samples were manufactured from the centre of the cylinder used to make the ring samples.

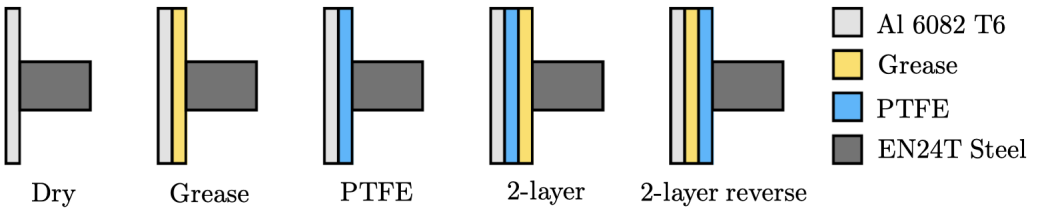


Figure 5: Diagram of the different lubrication configurations.

There are limited standards on the testing of FCs for metals with various lubrication options. The FC is determined from the ratio of the tangential and normal load that acts on the tested specimen. Therefore, both tangential and normal rigs would require load cells with control systems that provide stability and precision during the experiments [25]. The LFT is a simple method that could quantify the friction at the interface. The LFT utilised the Roell-Amsler HCT 25 tension/compression machine, as shown in Figure 6, which used the INSTRON 8800 series data logger.

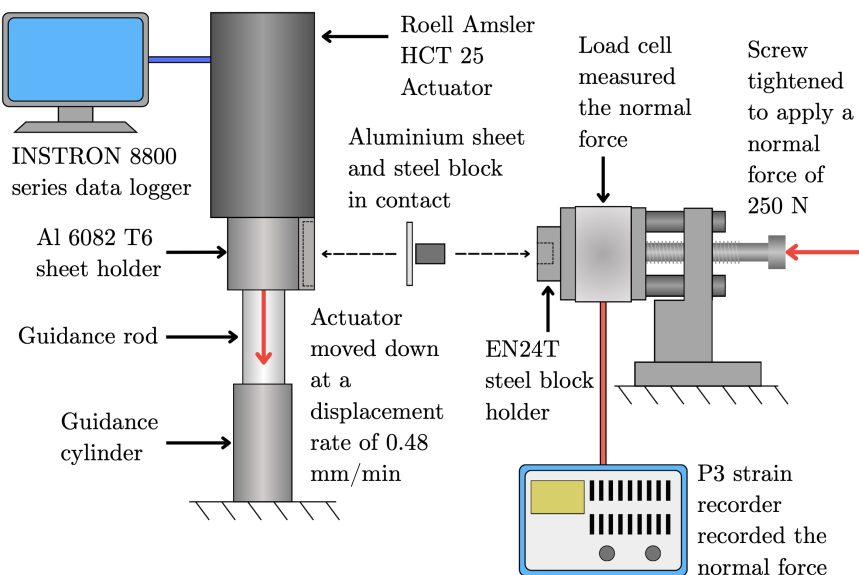


Figure 6: Diagram of the linear friction test setup.

The test rig, connected to the Roell-Amsler actuator, featured a rod that linked the actuator to the bottom apparatus, which would slide down the bottom apparatus during the test. The original rod did not provide a sliding fit, which would have introduced a systematic error into the results. This would have led to inaccuracies in the FC values, although it would not have affected their comparative relationship. To mitigate this issue, a new rod with a slide fit was manufactured, reducing the friction within the test setup that could have influenced the results. However, it remained possible that some residual systematic error could have persisted. The tangential force of the actuator was recorded by the INSTRON 8800 series data logger. The normal force was applied using the screw on the horizontal rig. This was measured by the VPG P3 Strain Indicator and Recorder, with the data being recorded throughout the experiment, which was analysed as discussed in Section 4.2.2.

The test procedure was applied as follows:

- The Roell-Amsler actuator was moved up to allow insertion of the Al 6082 specimen (40 × 25 mm, and thickness of 1.3 mm) and the EN24T steel cuboids (10 × 10 × 15 mm), with a contact area of 10 × 10 mm.
- The actuator was then moved down so that the specimens were aligned to be level, after the horizontal rig was secured.
- A normal force of 250 N was then applied using the screw in the horizontal rig, corresponding to a contact pressure of 2.5 MPa.

- The test was then performed using the INSTRON Wavematrix method, set to a relative ramp. The actuator moved downwards at a displacement rate of 0.48 mm/min. This was undertaken for a travelling distance of 4.8 mm, which was safely within the length of the specimen. The sample rate was set to 10 Hz to ensure sufficient data points were collected.
- The horizontal force applied was measured throughout the test since there were deviations from the initial force, this is further discussed in Section 4.2.2.

The LFT was required to match the conditions in the RHTT and therefore was undertaken in the Coulomb friction regime to ensure that the frictional behaviour between the aluminium and steel specimens was primarily affected by the normal force applied. Tests undertaken in the Coulomb friction regime can exhibit stick-slip behaviour as the specimen transitions between static and kinetic friction. However, this behaviour is typically less pronounced under steady sliding conditions. In order to maintain the Coulomb regime and ensure consistency with the RHTT, the same displacement rate of 0.48 mm/min was used. The low sliding velocity reduced the potential for velocity dependent effects. Additionally, an initial normal force of 250 N was applied to ensure the specimen remained in a sliding state. This combination of low velocity and a controlled normal force aimed to enable stable and accurate measurements of the frictional forces, whilst allowing for transitions between static and kinetic friction that are characteristic of the Coulomb regime.

4.2.2 Data Processing (WL)

Following the tests, actuator force data was extracted from the INSTRON 8800. Given that data acquisition was performed at 10 Hz at the specified displacement rate over a travelling distance of 4.8 mm, each series was comprised of 4800 tangential load measurements.

While the horizontal rig was intended to apply a constant normal force of 250 N, in practice this force was not constant and became increasingly negative throughout every test. Therefore, this required the use of the VPG P3 strain recorder to capture corresponding normal force measurements. However, the attempts to acquire real-time data via the recorder were unsuccessful. Instead, normal force values for each test were linearly interpolated over the range between the initial and final values, creating a synthetic array across all data points. Since the Wavematrix method applied a constant displacement rate with minimal acceleration, and the contact interface between the specimen and steel remained consistent throughout all tests, it was reasonable to assume a quasi-static system state. Under these assumptions, the FC for a specific test could then be directly calculated through the Coulomb friction relationship shown in Equation 1,

$$FC_{avg} = \frac{1}{m} \sum_{i=0}^m \frac{F_{t,i}}{F_{n,i}} \quad (1)$$

, where FC_{avg} is the average test FC, calculated using the ratio of tangential actuator force, F_t and the normal force F_n in N, for each measurement i over the array length m .

Across all tests, saw-tooth patterns were observed as a result of stick-slip behaviour. These waveforms can cause inconsistencies in the measured FC and lead to unpredictable behaviour when used in RHTT testing. Frequency analysis was used to capture the time-localised variations that could occur over the duration of an experiment, such as events where PTFE tape visibly snagged or tore. Quantifying these deviations provided an additional metric to select an appropriate lubrication option for the RHTT. Given the oscillatory nature of stick-slip behaviour, Fourier analysis was applied to analyse frequency components following work done by Xu et al. in 2022 [26]. Time-localised variations were captured by the bandwidth of dominant frequencies, where a broader range showed a more inconsistent stick-slip frequency. Signal drift was removed using a Savitsky-Golay filter, before extracting the frequency component of each signal using a Fast-Fourier Transform (FFT).

In order to quantify the severity of a single stick-slip event, a Continuous Wavelet Transform (CWT) was used. As with the FFT analysis, the signal trends were removed for stationarity. Using a Morlet

wavelet, a CWT was performed on a script following Equation 2,

$$\text{CWT}_{i,j}(x(t)) = \sum_m^{M-1} x_m \frac{1}{\sqrt{a_i}} \psi^\dagger \left(\frac{m-j}{a_i} \right), \quad a = \frac{f_\psi}{f \Delta t} \quad (2)$$

, where $x(t)$ is the actuator signal measured in N with M points, convoluted with the complex conjugate of the Morlet wavelet, ψ^\dagger . The indices i, j denote scaling indices over force amplitude and time measured in N and s, respectively. Additional parameters included the use of a dilation scale between $0 < a < 128$ and a sample rate of $\Delta t = 10$ Hz [27]. The resulting array $[i, j]$ corresponds to a coefficient at a particular point in scale and time. The coefficient amplitude, A , was taken as the maximum amplitude within the stick-slip frequency band. The average energy \bar{E} was calculated as the average sum of wavelet power over its total number of coefficients, as mathematically formulated in the Equation 3 below.

$$\begin{cases} A_{\text{wavelet}} = \max |\text{CWT}_{i,j}(x(t))| \\ \bar{E}_{\text{wavelet}} = \frac{1}{a+T} \sum_{a,t} |\text{CWT}_{i,j}(x(t))|^2 \end{cases} \quad (3)$$

For wavelet amplitudes, mean and standard deviations were first calculated for each individual waveform series to determine the average within a single test. These values were then further averaged across multiple test sets to obtain a representative wavelet amplitude. In contrast, wavelet energy was averaged only once across test sets, as the energy expression integrates contributions across the entire time domain of each waveform, providing a measure for each test without requiring further averaging.

4.3 Ring Hoop Tension Test (SC, WL)

The section below outlines the experimental methodology undertaken for the RHTT.

4.3.1 Experimental (SC)

GKN Aerospace utilises hemispherical metal spun components in hydrogen vessels designed for aircraft applications. The determination of the yield strength, UTS, and ductility of these tubular components is vital to assess the material's ability to withstand the stresses the component would encounter in service. This would enable the design of resilient components, increasing reliability and safety throughout its lifecycle to mitigate against the risk of failure.

The key parameters required to be investigated, as identified in Section 3, were the level of clearance and friction. In applications involving metal spun components, the tube diameter varies along axial length, complicating clearance control. The level of friction can be more easily adjusted through the use of lubrication. Therefore, this necessitates an understanding of the effect of clearance in comparison to the effect of friction on material property determination. These parameters were adjusted with the aim of understanding each factor's effect so that an experimental procedure could be developed for companies such as GKN Aerospace.

The inner diameter of the ring specimens was dictated by the overall length of the uniaxial specimens. The dimensions of the dog-bone on the ring specimen were identical to the UTT specimen but on a curved surface, as seen in Figure 7. After the uniaxial specimens had been obtained, as shown in Figure 2 in Section 4.1, the ring specimens were manufactured from the same solid cylinder of aluminium 6082 T6. This pipe was bored to a constant inner diameter of 101 mm, from which the ring specimens were then machined. The ring specimens can be assumed to be thin-walled since the ratio of wall thickness (2 mm) to internal radius (101 mm) is less than 0.1, so the assumption that radial stresses are negligible remains valid. Therefore, the ring specimen can be assumed to fail purely from hoop stresses. The manufacture of these specimens was limited, with only 20 aluminium 6082 T6 ring specimens made. The dog-bone gauge region had a 4:1 l:w ratio to promote uniform strain along the gauge length, which was in accordance with the ASTM E8 subscale specimen standards [13].

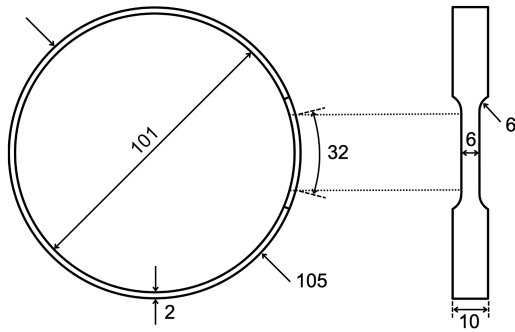


Figure 7: Engineering drawing of the ring tensile specimen, detailing its dimensions in mm .

A factorial style experiment was undertaken to investigate each combination of friction and clearance levels. Dry friction and lubricated setups were used. The lubricated option used was the Al-Grease-PTFE-Steel (2-layer reverse) setup since it had the lowest FC at 0.047, as seen in the LFT results in Section 6.2. The two sets of mandrels provided by GKN Aerospace had diameters of 49.2 mm (large clearance) and 50 mm (small clearance). Therefore, the two clearance options used were 1 mm (small) and 2.6 mm (large). The clearance also needed to provide sufficient capacity for the application of the lubricants. Four sets of tests were undertaken with five ring specimens tested for each, which were as follows:

- Set 1: Dry and Large Clearance.
- Set 2: Dry and Small Clearance.
- Set 3: Lubricated and Large Clearance.
- Set 4: Lubricated and Small Clearance.

The RHTT was set up as shown in Figure 8. The orientation of the ring relative to the mandrels remained consistent throughout each test. In order to balance friction reduction with optimal data acquisition for 3D-Digital Image Correlation (DIC) the gauge was positioned at 30°. As seen in Section 3.2.3, this placement was recommended to reduce the potential influences of frictional forces on material property determination whilst ensuring reliable strain measurements from the DIC.

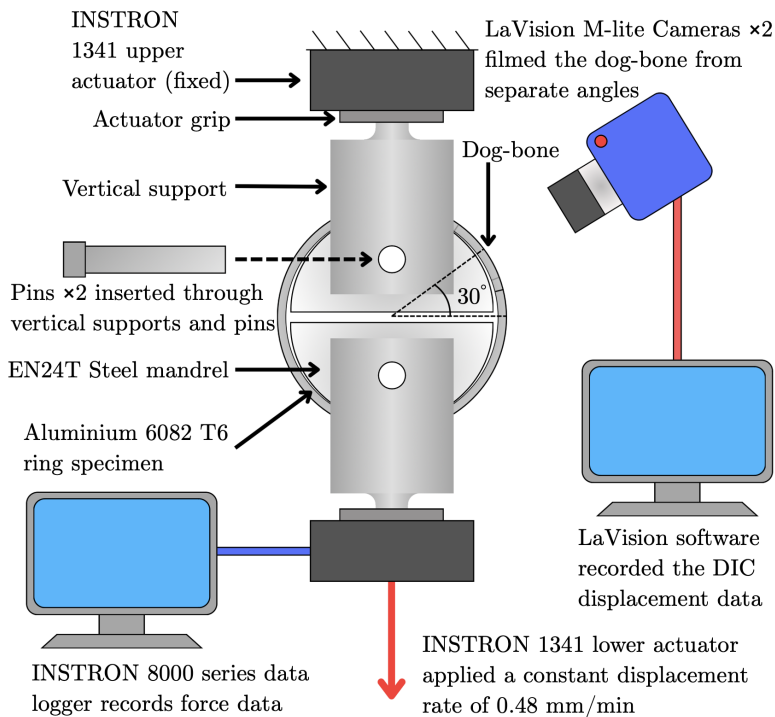


Figure 8: Diagram of the ring hoop tension test setup.

The method for each RHTT test, using the INSTRON 1341, was as follows:

- The RHTT experiment was set up as shown in Figure 8. The lower actuator of the INSTRON 1341 was moved down to remove any clearance, in order to place the specimen securely to reduce sliding and also decrease testing time. The specimen protect was then turned on.
- The test was then performed using the INSTRON Wavematrix method set as a relative ramp. The lower actuator was set to move down at a displacement rate of 0.48 mm/min, which was consistent with the UTT and was calculated in Section 4.1 in accordance with the ASTM E8 standards. The DIC recording was taken throughout the entirety of the test.
- The test was run until failure of the ring specimen.

In order to obtain displacement data for the ring specimen, DIC was used since it is able to obtain data in a 3D space [28]. The LaVision DIC StrainMaster Compact system used two Imager M-Lite 5 MP cameras, a DIC controller, and two LED lights to capture the data. The system was assembled so that the cameras were perpendicular to the dog-bone gauge region and then calibrated, as shown in Figure 8. The samples were prepared with a black and white speckled pattern that was spray painted onto the outer surface to provide reference points for the DIC. The DIC monitored the movement of the speckled pattern as the ring specimens were stretched, and the resulting data was obtained through analysis after recording. The data acquisition rate was set to 5 Hz, which was determined to be ample but was still limited due to the hardware's capability. A noise floor test was run for each set to ensure that the recording would have a sufficiently low level of noise.

Data was then obtained using the DIC post processing software, which ran the analysis of the recording. The first analysis processed the recording and the setting chosen was 'for speed', which provided a quicker but less robust analysis, where this was limited by the hardware capacity. The analysis region was redrawn for each recording to ensure the entire gauge region was analysed for each test. The second analysis measured the strain using a virtual extensometer, which was placed in the centre of the dog-bone region and had a gauge length of 25 mm as per the ASTM E8 standards [13]. The displacements were also obtained for two allocated strain gauge zones, with their centres placed at either end of the virtual extensometer.

4.3.2 Data Processing (WL)

Data processing of the RHTT was performed in similar fashion to its uniaxial counterpart, but with some complexities. The actuator force column was extracted directly via the channel 1 Load ADC 1 recording. The load was halved to account for the effective load being shared between two actuators. In Section 4.3.1, both the virtual extensometer displacement and the tracked strain gauge zone measurements were obtained. Total strain was calculated using 3D local displacement data computed within the area tracked by each of the two strain gauge zones. By using Equation 4, the Euclidean distance was calculated for each gauge area for each x, y , and z direction, then summed to calculate a total strain:

$$\varepsilon_i = \left\| \frac{\vec{r}_{1,i}}{\vec{r}_{1,0}} \right\|_2 + \left\| \frac{\vec{r}_{2,i}}{\vec{r}_{2,0}} \right\|_2, \quad \forall r_{1/2,0,j} \neq 0 \quad (4)$$

, where $\vec{r}_i = [x_i, y_i, z_i]^\top$ denotes the directional displacements in mm, indexed at position i and subscripted with either 1 or 2 to denote the gauge. $\|\cdot\|_2$ represents the Euclidean norm. Under the assumptions of a thin-walled and a uniform contact regime, the effective hoop stress was calculated via Equation 5,

$$\sigma = \frac{F \tan(\theta)}{2tw} \quad (5)$$

, where F is the recorded actuator load in N. t, w are wall thickness and axial width respectively measured in mm, used to define the cross-sectional area acted on in the hoop direction. θ is the angle between the vertical and the direction of hoop stress. Given that the mandrel had a semicircular profile, the effective average angle over the contact region spanned was 45° . Average stress-strain curves were produced for each combination of clearance and lubrication configuration for visual comparison, following a similar procedure to 4.2.2. The resulting averaged curves were then truncated at the average

failure strain value to ensure the plot was representative of the average ductility. The values of yield strength and UTS were calculated for further analysis.

4.4 FE Modelling (TJC, DL)

The rationale for FE modelling was to investigate the impact of various parameters on the RHTT response. The use of FE modelling enabled the simulation of more loading cases than those used experimentally and also eliminated limitations such as sample size constraints, available resources and time. Friction and clearance were investigated in greater depth, since literature indicated that these parameters have the greatest impact on results, as discussed in Section 3.2. Their effect was further validated through the experimental test results as detailed in Section 6.3.

Another advantage of FE modelling is a greater precision in controlling these parameters. Since achieving specific friction levels in the experiments was not feasible, the FE model was designed to assess the impact of friction, which included sensitivity testing. Additionally, FE modelling enabled investigation of a wider range of clearance levels, whereas in the physical experiments, only two clearances could be tested since manufacturing multiple rings or mandrels of varying sizes conflicted with time constraints.

Two types of model were created: a model to simulate the UTT and another for the RHTT. The objective of the UTT model was to ensure the input material data, from the experimental UTTs, was accurate, and to confirm whether the model could sufficiently replicate simple tests. The main objective of the RHTT model was to enable further investigation of influential factors such as ring-mandrel friction level and clearance.

For both FE models, the key material tensile properties extracted were the yield strength and UTS. Since the models did not feature a damage characterisation, they were limited to capturing deformation behaviour and could not provide insight into the progression of fracture and the material's ductility. However, as discussed in Section 3.1, the ductility measured in the RHTT is only an indication of the material's ductile response, rather than a precise value. Therefore, obtaining its value through FE modelling was not essential within this investigation.

Material definitions: Sections were created for EN24T steel and Al 6082 T6. The elastic properties and densities for these materials are provided in Table 1. For both materials, mass density was considered uniform whilst elasticity was considered isotropic.

Table 1: Material properties input to Abaqus/CAE [29][30].

Material	Density ρ (kg/m ³)	Young's modulus E (GPa)	Poisson's Ratio ν
EN24T Steel	7850	200	0.30
Al 6082 T6	2700	70	0.33

The plastic behaviour of Al 6082 T6 was modelled through isotropic hardening with linear extrapolation. This minimised computational expense whilst accurately modelling behaviour under monotonic loads. The use of more complex hardening models would only be necessary for capturing cyclic loading phenomena such as the Bauschinger effect [31], so this was not done. Plasticity was defined via a look-up table containing 60 yield strength points and 60 plastic strain data points derived from Figure 9, which shows an averaged and extrapolated curve calculated from the experimental UTT stress-strain responses presented later in Section 6.1. An average curve accounted for the variability within the five performed UTT tests. The plastic region was extrapolated past the point of failure, neglecting necking in order to provide appropriate material data for simulation purposes.

The plastic behaviour of the EN24T steel was defined by a high yield strength of 586 MPa [29], effectively rendering the steel components non-deformable. The methodologies for configuring the UTT and RHTT FE models are detailed in the following subsections.

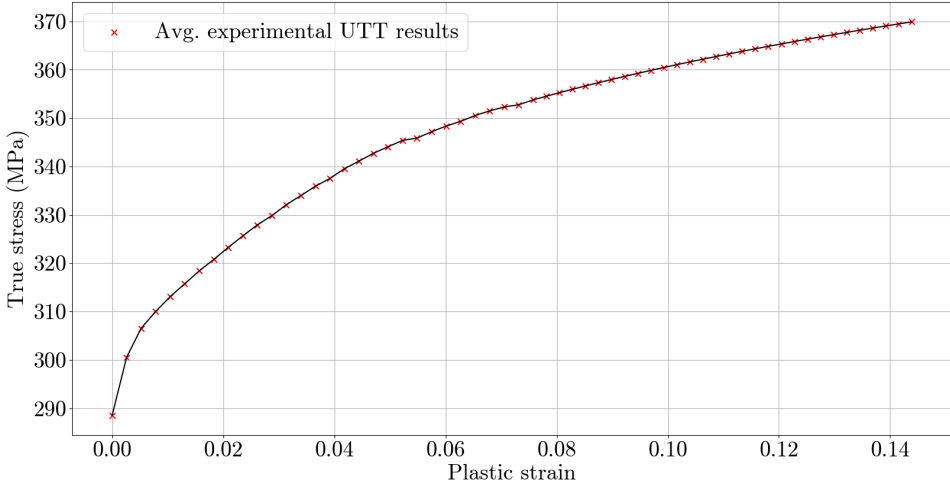


Figure 9: Data points taken from the plastic region of the averaged experimental UTT curve.

4.4.1 UTT FE Model (TJC)

Component generation: This simple model consisted of a single uniaxial dog-bone specimen. This was designed within Fusion 360 with dimensions as specified in Section 4.1. The design was subsequently imported into Abaqus/CAE as a STEP file to generate a 3D deformable solid which was assigned the previously described Al 6082 T6 material section.

Boundary conditions: Two Boundary Conditions (BCs) were applied to the UTT specimen. The first was created in the initial step, and was applied on the top surface of the gauge specimen, restricting its movement entirely by specifying ($U_1 = U_2 = U_3 = 0$), since this was held stationary throughout the experiment as described in Section 4.1. The second BC was applied in the subsequent Step-1 on the lower surface of the specimen. This specified a constant downward velocity of -8 mm/s in the tensile z -direction, replicating the displacement rate of 0.48 mm/min applied experimentally in Section 4.1. These boundary conditions are illustrated in Figure 10a.

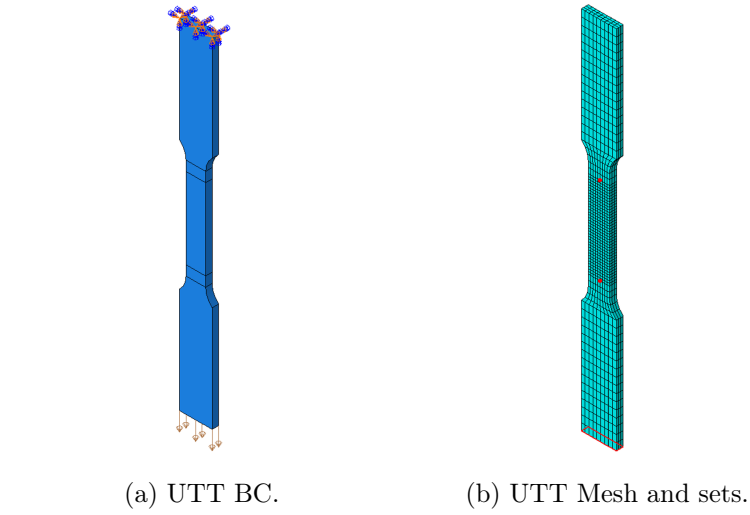


Figure 10: Boundary conditions imposed on the UTT model in Abaqus/CAE.

Meshing strategy: The UTT specimen was meshed with a finer seed within the constant-width gauge region of interest. The rest of the component, consisting of the grips and curved region of the dog-bone, featured a coarser mesh with a size three times that of the gauge section, as illustrated in Figure 10b. This conserved computational resources whilst providing an adequately smooth transition between the two mesh sizes. The pair of nodes, highlighted in Figure 10b, were used later for the extraction of strain values, serving as the ends of a virtual strain gauge. A mesh convergence study was conducted

to optimise element shape and size for accuracy in the model's results using the global maximum von Mises stress as the comparison point. The results of the convergence study are presented in Figure 11. Linear elements were deemed appropriate for modelling the deformation of the UTT specimen, as they conserved computational resources with only a minimal difference compared to that of the results obtained using quadratic elements. This was possible due to the specimen's simple and flat geometry. Figure 11 indicated that a linear hexahedral C3D8 element converged the quickest to the value of 369.5 MPa. This element type was selected, with a global seed size of 2 mm and a local gauge seed size of 0.667 mm, optimally balancing computational efficiency with accuracy.

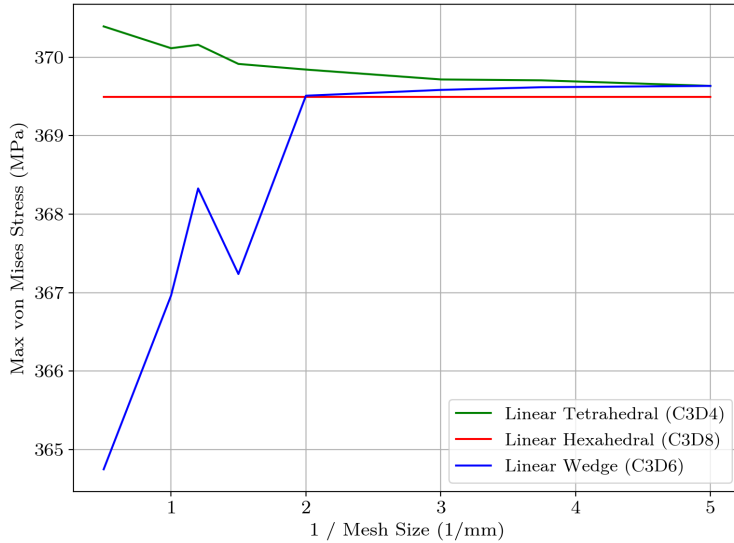


Figure 11: Mesh convergence for UTT FE model.

Step settings: To calculate the necessary step time for the simulation to correspond with the experiments, the mean actuator displacement for the experimental UTTs (2.84 mm) was divided by the velocity applied in the downwards direction (-8 mm/s). This gave a step time of 355 s. Given the simplicity of the model, a maximum number of increments of 100 was selected.

4.4.2 RHTT FE Model (DL)

Component generation: The RHTT model featured two identical EN24T steel mandrels and the Al 6082 T6 ring specimen, which were all modelled as 3D deformable solids. The mandrels were created within the Abaqus/CAE part module, with diameters of 96-101 mm assigned to achieve different ring-mandrel clearances in various models. To replicate the mandrel components used experimentally, the parts also included a 12.7 mm through hole. Due to its relatively complex geometry, the ring specimen was imported directly from Fusion 360 as a STEP file. The ring geometry was kept constant across all models. Due to the symmetrical nature of the RHTT setup, each component was halved along the xz -plane to reduce computational expense, since all output fields would be mirrored about this plane within a full model.

Assembly and boundary conditions: Independent instances for each component were added to the assembly. The ring instance was rotated about the y -axis to orientate the dog-bone centre 30° from the horizontal xy -plane, emulating the experimental setup. It was then translated to balance on the top of the upper mandrel, leaving a clearance between the lower mandrel and the ring, as was done experimentally. Since all components were half-models of real parts, the flat annular surface of the ring was arranged to sit in-plane with the flat semicircular mandrel faces on the central xz -plane of symmetry as shown in Figure 12a. As previously mentioned, a y -symmetry boundary condition was imposed in the initial step on these surfaces as shown in Figure 12a, constraining y -direction movement and rotation about the x - and z -axes. The upper mandrel was constrained from the initial step in all directions with a $U_1 = U_2 = U_3 = 0$ BC placed on its curved face as shown in Figure 12b. In the following Step-1, a velocity BC of -8 mm/s was applied in the tensile z -direction on the curved face

of the lower mandrel as shown in Figure 12c. This emulated the constant displacement rate of 0.48 mm/min used experimentally, derived in Section 4.1.

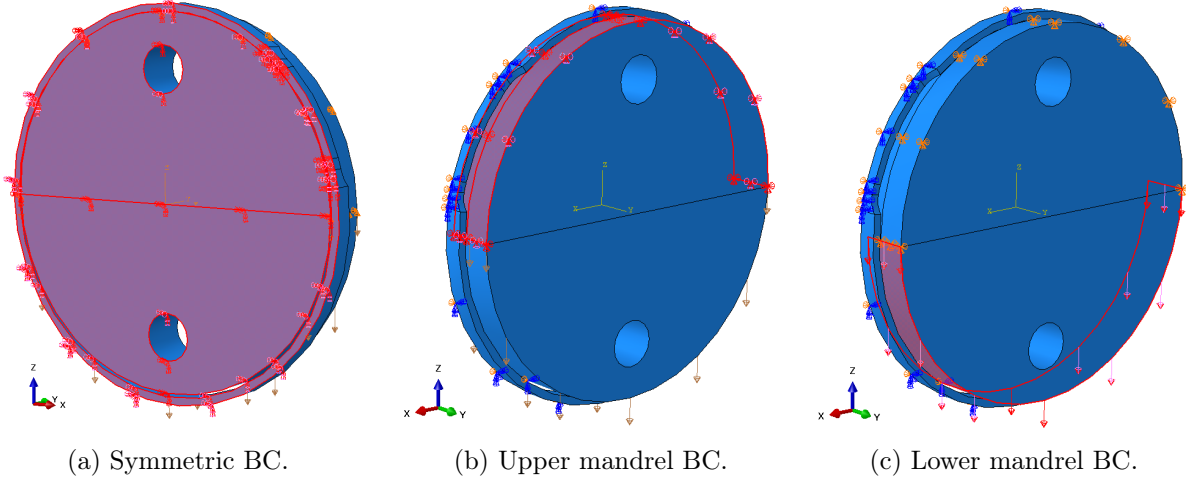


Figure 12: All boundary conditions imposed on the model in Abaqus/CAE.

The curved mandrel surfaces were arbitrarily selected for the latter two boundary conditions since the mandrels effectively moved as rigid bodies. Selection of alternative surfaces for these conditions was equally valid and did not yield different results.

Friction modelling: A friction interaction property was defined in the interaction module. Its tangential behaviour was defined via a penalty friction formulation with isotropic directionality, whilst normal behaviour was modelled by ‘Hard’ contact. The penalty formulation was found to be far more stable than the Lagrange multiplier alternative, reducing the size of system matrices and thus computation time. This enabled far quicker convergence during simulation. A friction contact was then defined between the curved surfaces of the mandrels and the inner surface of the ring specimen. A small sliding formulation was deemed appropriate since the relative motion between the interacting surfaces is minimal. Surface-to-surface discretisation ensured accurate force distribution over contact regions, and avoided the occurrence of stress singularities associated with node-to-surface discretisation.

Meshing strategy: The ring specimen was partitioned into three mesh zones, consisting of the central 25 mm gauge section, the remainder of the dog-bone section up to the end of the fillets, and the main body of the ring outside of the dog-bone. As shown in Figure 13a, the meshing scheme featured a 1:2:4 ratio between mesh sizes within the gauge, dog-bone and global regions. This facilitated a gradual transition from the larger global mesh to the finer gauge region mesh, which minimised stress concentration artifacts associated with abrupt changes in mesh size. Most importantly, this enhanced accuracy in the gauge section. Figure 13b shows the local mesh generated around the dog-bone contact region. The highlighted pair of nodes marked the ends of a virtual strain gauge, which will later be used to measure strain in a similar manner to that mentioned in Section 4.4.1.

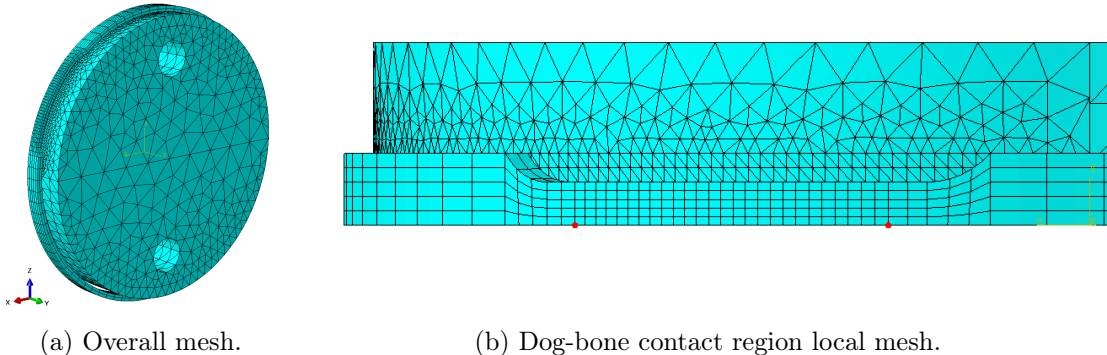


Figure 13: Visualisations of the mesh generated on the model, from Abaqus/CAE.

The steel mandrels were found to be most optimally modelled using quadratic tetrahedral C3D10 elements, which reduced computation time the most compared to other element shapes. Figure 13a shows that the rounded contact surfaces of the mandrels were meshed to match the global ring size, ensuring a similar number of nodes on both surfaces. Similarly, Figure 13b shows that part of the upper mandrel was meshed to match the size within the gauge section. Matching node densities on both contact regions ensured interactions were modelled accurately. The rest of the mandrel was meshed with a global size $2.5 \times$ larger than the global size on the ring, as these regions were considered to be less important. Following a mesh convergence study, it was found that the quadratic hexahedral C3D20 elements were most suitable for modelling the ring component, with a gauge section local mesh size of 1 mm selected as optimal as demonstrated by Figure 14.

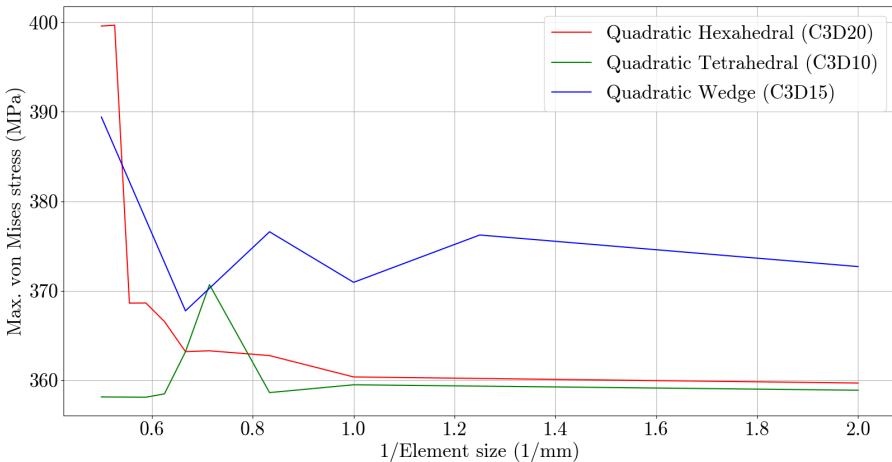


Figure 14: Results of convergence study for gauge section elements.

In accordance with the previously determined ratios, this resulted in seed sizes of 2 mm on the remainder of the dog-bone, 4 mm on the main ring body and the mandrel contact surfaces, 10 mm on the main mandrel bodies, and 1 mm in the upper mandrel contact region with the dog-bone. The use of quadratic elements on all components was crucial to suitably approximate the curved contact surfaces, given that the use of their linear counterparts resulted in severe convergence issues. The matching of node densities on all regions of the contact surface was essential to ensure the accurate modelling of the contact interaction.

Step settings: A static, general step named Step-1 was created to follow the initial step, with non-linear geometry (NLGEOM) toggled on. This was appropriate since the tensioned ring specimen experienced significant deformation during the test. Though less computationally expensive, a linear assumption fails to account for the resulting geometric changes in stiffness due to stretching, which are essential to the analysis of thin rings under large deformations in a RHTT. The step time was set to a standard 600 s duration for initial simulations. A maximum of 1000 increments and a minimum increment size of 1×10^{-10} were found necessary to achieve consistent convergence across all models. Auto-stabilisation was required to ensure consistent convergence across all simulations. This was specified as a dissipated energy fraction of 5% to prevent divergence by introducing a form of numerical damping. This was minimised to reduce the effect of artificial damping on simulation results, though this was found to be relatively insignificant.

4.4.3 Extraction of Tensile Responses (DL)

For both models, it was essential to extract tensile responses using the same procedure as was used for the experimental data in Section 4.3.2, to enable direct comparison. In both models, the field output request was limited to the logarithmic strain, von Mises stress, displacement, and z-component reaction force RT3 to preserve computational resources. Output data was written in 5-second increments to define a sufficiently well defined stress-strain response whilst minimising computational cost and ensuring incremental uniformity and comparability across all simulated output files.

Upon completion of simulations, stress-strain responses were extracted from the resulting Output Database (ODB) files in the visualisation module. In line with Section 4.3.2, it was appropriate to calculate stress using the actuator force, F , as was done experimentally, rather than use the stress field output within the ODB. For the UTT model, F was found from the ODB as the sum of the absolute reaction RT3 force in the tensile z -direction over the surface on which the velocity BC was applied, shown in Figure 10a. The engineering stress was found from the UTT model ODB by dividing this force by the gauge section area 12 mm².

From the RHTT model, RT3 was instead summed over the mandrel contact face highlighted in Figure 12c to find the applied actuator force. Given that a half-model was used in the case of the RHTT model, this force must be doubled to provide the full actuator force F . However, in accordance with the analytical model presented in Section 5, $F/2$ is exerted on each side of the ring and used to calculate stress through a section. As such, the summed RT3 force within the RHTT half-model was used directly as $F/2$, which was then divided by the gauge cross-sectional area to provide the engineering stress.

To emulate the experimental strain measurement described in Section 4.3.2, the displacements of two nodes at the ends of the gauge region were tracked. These pairs of nodes are shown in red within Figures 10b and 13b for the UTT and RHTT models respectively. These nodes are analogous to the two strain gauge regions used experimentally in Section 4.3.2. In the case of the RHTT, displacements at these nodes were sufficiently small to ignore their slight curvature and directly use absolute displacement rather than calculating their circumferential equivalents. The displacements at each node were summed at each time increment to provide their combined displacement from their initial positions. This was then divided by 25 mm, the initial gauge length for both models, to provide engineering strain.

5 RHTT Analytical Stress Model (DG)

As mentioned in Section 3.2.3, the presence of friction between the hemispherical mandrels and the ring specimen in RHTTs results in hoop stress non-uniformity across the dog-bone. This section derives the stress distribution across the dog-bone and an adjustment factor to correct the experimental results at varying FCs. The results of this analytical model were also used to validate the behaviour of the FEA.

5.1 RHTT Analytical Stress Model Assumptions

Following the approach of a similar analytical model by Khalfallah et al., this model was constructed on the assumption of no clearance and constant contact between the ring and the mandrels, in order to exclude the complex behaviour introduced by bending [32]. The addition of PTFE and grease when using a small clearance resulted in a tight fit, which meant the effect of bending was considered negligible on the stress distribution. Under this assumption, the mandrels sustain the original curvature of the ring, neglecting the effects of bending. In practice, the ring experiences bending when it is not in contact with the mandrels and a gap zone forms, as seen in Figure 15. The results detailed in Section 6.3.2 showed the effect of bending due to larger clearances was non-negligible.

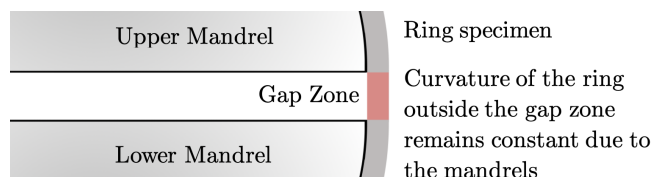


Figure 15: Diagram of the curvature of the ring in the gap zone.

During testing, the gap zone was observed to be small and the curvature of the ring within it was relatively unchanged. Additionally, as the dog-bone never fell within the gap zone during testing, bending was considered to have a negligible effect on the dog-bone stress distribution.

5.2 RHTT Hoop Tensile Force Derivation

The applied force acted vertically through the centre of the ring and the mandrels. The cross-sectional area of the ring was constant, excluding the dog-bone. Therefore, the tensile force at $\theta = 0$ and $\theta = \pi$ radians was equal to half the actuator force. Similarly, the tensile forces at $\theta = \frac{\pi}{2}$ and $\theta = \frac{3\pi}{2}$ were the same, but not equal to half the actuator force. Therefore, the maximum value of angle θ was restricted to $\frac{\pi}{2}$, so only a quarter of the setup was considered as part of a force diagram [32].

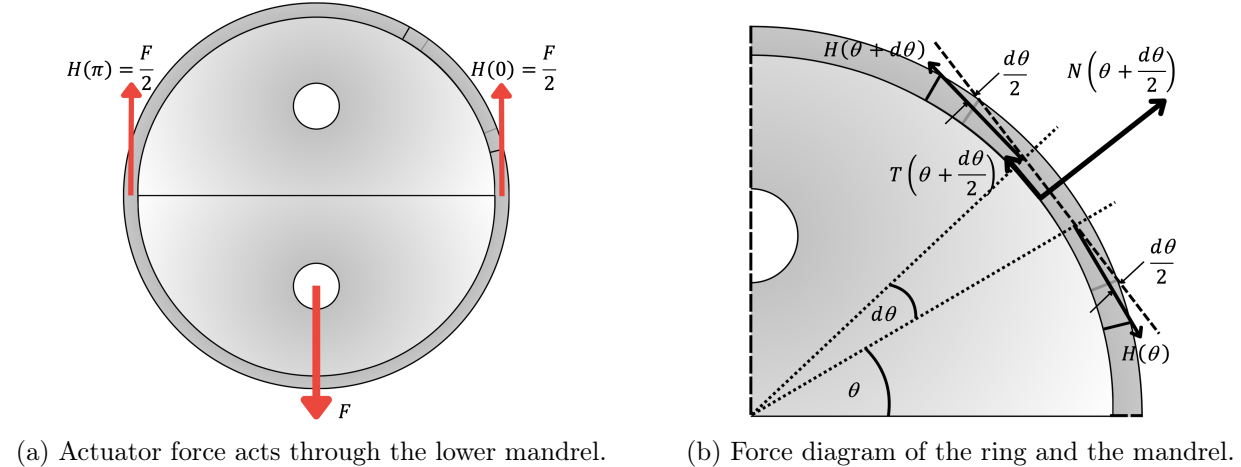


Figure 16: Forces acting upon the ring and mandrels during testing.

From Figure 16b, a force balance resulted in the following system of equations:

$$N\left(\theta + \frac{d\theta}{2}\right) - H(\theta + d\theta) \sin\left(\frac{d\theta}{2}\right) - H(\theta) \sin\left(\frac{d\theta}{2}\right) = 0, \quad (6)$$

$$T\left(\theta + \frac{d\theta}{2}\right) + H(\theta + d\theta) \cos\left(\frac{d\theta}{2}\right) - H(\theta) \cos\left(\frac{d\theta}{2}\right) = 0, \quad (7)$$

where $H(\theta)$ is the hoop tensile force, $N(\theta)$ is the normal force, and $T(\theta)$ is the tangential force all in N, considered for an infinitesimally small section of the ring. As the normal and tangential forces are orthogonal to each other at the interface between the ring and the mandrels, Coulomb's law of friction was applied:

$$T\left(\theta + \frac{d\theta}{2}\right) = \mu N\left(\theta + \frac{d\theta}{2}\right), \quad (8)$$

where μ is the FC. Let $H(\theta) = H$ and $H(\theta + d\theta) = H + dH$. Substituting Equation 8 into Equation 7 and rearranging for $N(\theta)$, then combining with Equation 6 allowed for the elimination of $N(\theta)$:

$$\frac{H + dH}{\mu} \cos\left(\frac{d\theta}{2}\right) - \frac{H}{\mu} \cos\left(\frac{d\theta}{2}\right) + (H + dH) \sin\left(\frac{d\theta}{2}\right) - H \sin\left(\frac{d\theta}{2}\right) = 0. \quad (9)$$

Using small angle approximations, $\sin(d\theta) \approx d\theta$ and $\cos(d\theta) \approx 1 - \frac{d\theta^2}{2}$:

$$\frac{H + dH}{\mu} \left(1 - \frac{d\theta^2}{8}\right) - \frac{H}{\mu} \left(1 - \frac{d\theta^2}{8}\right) + (H + dH) \frac{d\theta}{2} - H \frac{d\theta}{2}, \quad (10)$$

eliminated higher order terms $d\theta^2$ and $d\theta dH$ since they are infinitesimally small. This simplified to:

$$\frac{dH}{\mu} + Hd\theta = 0, \quad (11)$$

which was rearranged and then integrated between the arbitrary angle $\theta = \phi$ and $\theta = 0$:

$$\int_{H(0)}^{H(\phi)} \frac{dH}{H} = - \int_0^\phi \mu d\theta, \quad (12)$$

$$H(\phi) = H(0)e^{-\mu\phi}, \quad 0 \leq \phi \leq \frac{\pi}{2}, \quad (13)$$

where Equation 13 is known as the Capstan Equation. The hoop tensile force at $\phi = 0$ was equal to half the applied actuator force on the lower mandrel:

$$H(\phi) = \frac{F}{2}e^{-\mu\phi}, \quad 0 \leq \phi \leq \frac{\pi}{2}, \quad (14)$$

where F is the applied actuator force in N. The $e^{-\mu\phi}$ term is the Capstan adjustment factor which corrects for friction due to the angle of the dog-bone in RHTT, detailed later in Section 6.3.2.

5.3 RHTT Dog-bone Cross-sectional Area Derivation

The hoop stress across the dog-bone is dependent on the changing cross-sectional area of the dog-bone:

$$\sigma(\phi) = \frac{H(\phi)}{A(\phi)} = \frac{H(\phi)}{t \cdot w(\phi)}, \quad 0 \leq \phi \leq \frac{\pi}{2}, \quad (15)$$

where, $\sigma(\phi)$ is the hoop stress in Pa, t is the constant thickness of the ring in m, and $A(\phi)$ is the cross-sectional area of the ring in m^2 , which is dependent on $w(\phi)$, the width of the dog-bone in m which is constructed from the dimensions shown in Figure 17.

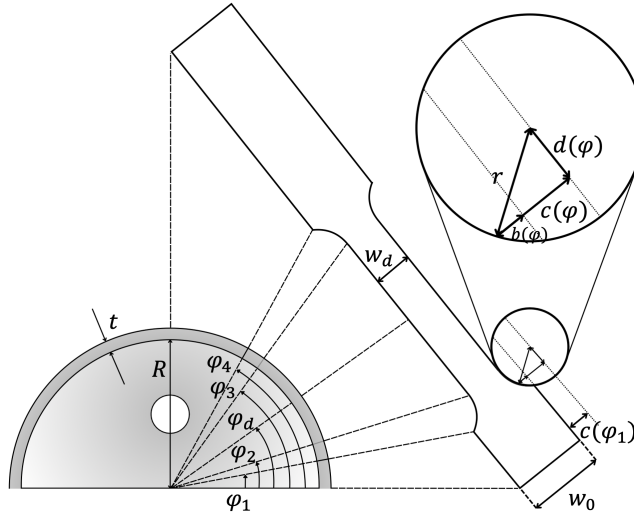


Figure 17: Diagram detailing the angles that dictate the changing cross-sectional area of the dog-bone.

The width $w(\phi)$ of the ring throughout the dog-bone was defined as:

$$w(\phi) = w_0 - 2b(\phi), \quad 0 \leq \phi \leq \frac{\pi}{2}, \quad (16)$$

where w_0 is the nominal width of the ring and $b(\phi)$ is half the effective chord length of the dog-bone fillet, all in m. Using the system of dimensions seen in Figure 17, $b(\phi)$ was defined as:

$$b(\phi) = c(\phi) - c(\phi_1) = \sqrt{r^2 - d(\phi)^2} - c(\phi_1), \quad 0 \leq \phi \leq \frac{\pi}{2}, \quad (17)$$

where $c(\phi)$ is half the chord length of the dog-bone fillet, r is the radius of the dog-bone fillet, $d(\phi)$ (defined in Equation 21) and $c(\phi_1)$ are dimensions all in m, shown in Figure 17. $c(\phi_1)$ was defined as:

$$c(\phi_1) = r - \frac{w_0 - w_d}{2}, \quad (18)$$

where w_d is the width of the dog-bone in m. Setting $\phi = \phi_1$ in Equation 17 resulted in the following:

$$d(\phi_1) = \sqrt{r^2 - c(\phi_1)^2}. \quad (19)$$

The angles defining the position of the dog-bone relative to the mandrels in Figure 17 were defined as:

$$\begin{cases} \phi_1 = \phi_2 - \frac{d(\phi_1)}{R} \\ \phi_2 = \phi_d - \frac{L}{2R} \\ \phi_3 = \phi_d + \frac{L}{2R} \\ \phi_4 = \phi_3 + \frac{d(\phi_1)}{R}, \end{cases} \quad (20)$$

where ϕ_1 , ϕ_2 , ϕ_3 and ϕ_4 , seen in Figure 17, are the angles defining the position of the dog-bone relative to the mandrels, L is the length of the flat section of the dog-bone and R is the inner radius of the ring specimen, all in m. Therefore, $d(\phi)$ was defined for intervals based on angles ϕ_1 , ϕ_2 , ϕ_3 and ϕ_4 :

$$\begin{cases} d(\phi) = d(\phi_1) & , \quad 0 \leq \phi \leq \phi_1 \\ d(\phi) = R(\phi_2 - \phi) & , \quad \phi_1 \leq \phi \leq \phi_2 \\ d(\phi) = 0 & , \quad \phi_2 \leq \phi \leq \phi_3 \\ d(\phi) = R(\phi - \phi_3) & , \quad \phi_3 \leq \phi \leq \phi_4 \\ d(\phi) = d(\phi_1) & , \quad \phi_4 \leq \phi \leq \frac{\pi}{2}. \end{cases} \quad (21)$$

Overall, the equations defining the area of the dog-bone allowed for the visualisation of the stress distribution across the dog-bone, which was compared to the stress distribution predicted by the FE model, seen later in Section 6.4.2. The Capstan adjustment factor $e^{-\mu\phi}$, derived in Section 5.2 was applied to the experimental RHTT results to correct for the friction due to the angle of the dog-bone, detailed later in Section 6.3.2.

6 Results

6.1 Uniaxial Testing (DG)

The engineering stress-strain curves for each test were plotted, as seen in Figure 18. The Young's modulus, yield strength, UTS, and ductility were all derived using the methods detailed in Section 4.1.

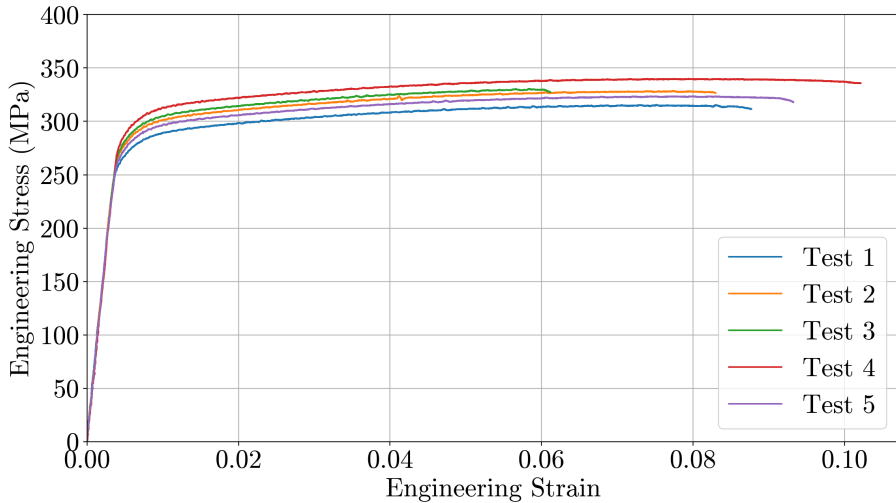


Figure 18: Engineering stress-strain curves of each uniaxial tensile test.

From Figure 18, it is clear that the specimens exhibited similar elastic behaviour and only deviated in the plastic region. This behaviour is summarised by the mean and the associated standard deviations of the material properties shown in Table 2.

Table 2: Uniaxial Tension Test mean results.

Young's modulus (GPa)	Yield Strength (MPa)	UTS (MPa)	Ductility (%)
70 ± 0.99	287 ± 8.12	328 ± 8.09	8.54 ± 1.37

The Young's modulus had the smallest coefficient of variation (standard deviation as a percentage of the mean) of $\pm 1.41\%$. The yield strength and UTS of 287 MPa and 328 MPa also had relatively small coefficients of variation of $\pm 2.83\%$ and $\pm 2.47\%$ respectively. However, there was significant variability in ductility from 6% to 10%, which resulted in the largest coefficient of variation of $\pm 16.04\%$.

6.2 Linear Friction Testing (SC, WL)

The results obtained for the LFT are presented below, which were then analysed to determine the best lubricant for utilisation in the RHTT.

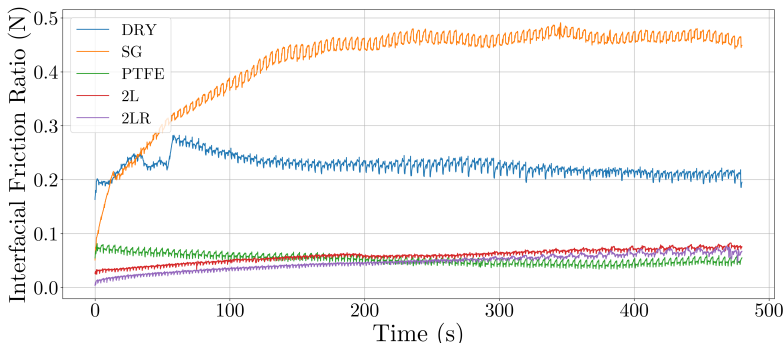
6.2.1 Friction Coefficient Results (WL, SC)

Table 3 shows the mean FC and its standard deviation for each lubrication option. A representative test from the experimental data, for each lubrication option, is shown in Figure 19a. The experimental FC was calculated as discussed in Section 4.2.2, using no lubrication (Dry) as the baseline for comparison with the other lubrication options. The five lubrication options evaluated were: Al-Dry-Steel (dry), Al-Grease-Steel (SG), Al-PTFE-Steel (PTFE), Al-PTFE-Grease-Steel (2-layer), Al-Grease-PTFE-Steel (2-layer reverse).

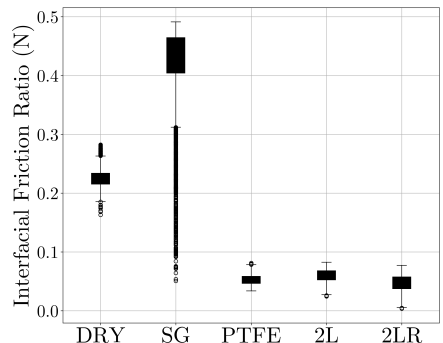
Table 3: Measured FC for different lubrication options.

Lubrication Option	Friction Coefficient
Dry	0.256 ± 0.022
Silicone grease	0.402 ± 0.075
PTFE	0.0546 ± 0.020
2-layer	0.0650 ± 0.0072
2-layer reverse	0.0471 ± 0.0084

Table 3 shows that the lubrication option with the lowest FC was the 2-layer reverse configuration with a value of 0.0471. This configuration reduced the FC by over five times more than the dry option. It is apparent that in lubrication conditions where steel was in contact with grease, the FC was negatively impacted, as shown by the FC obtained with the SG and the 2-layer option (2L). With solely grease, the FC was measured to be 0.402 with a standard deviation of 0.075, which was higher than the dry tests. This is shown in the box plot for 'SG' in Figure 19b, where a greater interquartile range and a larger number of outliers were observed. The standard deviations of the FCs in Table 3 shows the consistency of the results for each lubrication option. This showed that configurations with multiple layers had the most repeatable configuration. Both 2-layer options had a standard deviation of 10 times less than the single or dry arrangements. While PTFE alone provided the second lowest FC, its standard deviation was higher than the 2-layer reverse, making it less reliable for RHTT testing.



(a) Representative stick-slip series for each test.



(b) Boxplot of FC distribution.

Figure 19: Linear friction test results.

6.2.2 Wavelet Analysis Results (WL)

While standard deviations across tests in Table 3 demonstrate the consistency of FC results for a given lubrication option, they do not account for the consistency of a measured FC within a given test.

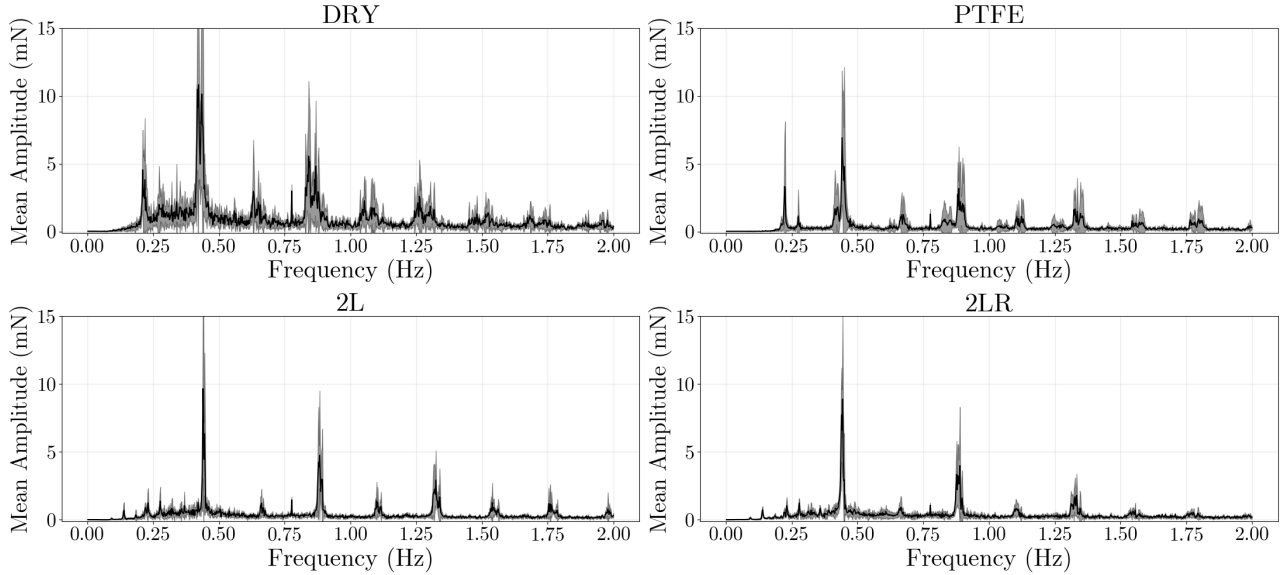


Figure 20: Lubrication option Fourier frequency analysis.

The results of FFT analysis in Figure 20 showed various frequency spectra which represented the frequencies associated with periodic stick-slip behaviour for each test type. Dominant peaks were observed at the characteristic stick-slip frequency, along with smaller spikes along corresponding harmonics. In the 2-layer configurations, these excited frequencies had smaller bandwidths and pronounced spikes, which showed smaller frequency deviations in the dominant frequency along with its harmonics. This indicated stronger periodicity and thus less stick-slip frequency variation throughout a test. In contrast, with the dry and single-layer frequency spectra, there was less consistent behaviour and an increased randomness of events observed. These large events are likely the result of strong interactions between direct metal-metal interfaces in dry scenarios, or visible physical events such as tearing or snagging caused by the use of PTFE tape.

Table 4: Average wavelet component analysis.

Lubrication Option	Integrated Energy ($10^{-5} N$)	Max Coefficient Amplitude ($10^{-3} N$)
Dry	4.47 ± 2.29	4.15 ± 1.17
Silicone grease	4.44 ± 3.54	4.15 ± 2.25
PTFE	1.18 ± 0.90	2.21 ± 0.99
2-layer	0.91 ± 0.31	1.84 ± 0.41
2-layer reverse	0.77 ± 0.17	1.65 ± 0.201

A high average maximum coefficient amplitude indicated an inconsistent FC measurement throughout any given test. This metric quantified the severity of a slip event, with higher amplitudes tending to artificially increase the instantaneous friction at a slip event. Through summing the amplitudes across the entire waveform, the integrated wavelet energy measured the strength of such slip events in the context of the energy dissipated throughout the test, with a higher value associated with either energetic and/or frequent slips. The amplitude and energy measurements can be interpreted as the effective standard deviation over the time domain. Lower amplitudes and energies yielded more consistent instantaneous FC results, which indicated a more reliable RHTT setup. Table 4 shows the different wavelet energies and coefficient amplitudes for each testing scenario, with the standard deviation across each test being recorded. As the Al-Grease-PTFE-Steel (2-layer reverse) option was shown to have the

smallest of both of these metrics, this further justified the choice for its use as the preferred lubricant option for the RHTT.

6.3 Ring Hoop Tension Test (SC, DG)

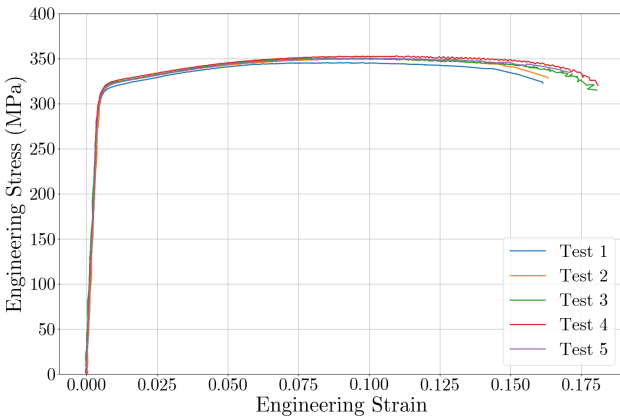
The results obtained from the RHTTs, which show the apparent engineering stress and strain, are seen in the following section. The Capstan adjustment was then applied, detailed in Section 6.3.2, to provide results that were adjusted for friction.

6.3.1 Original Results (SC)

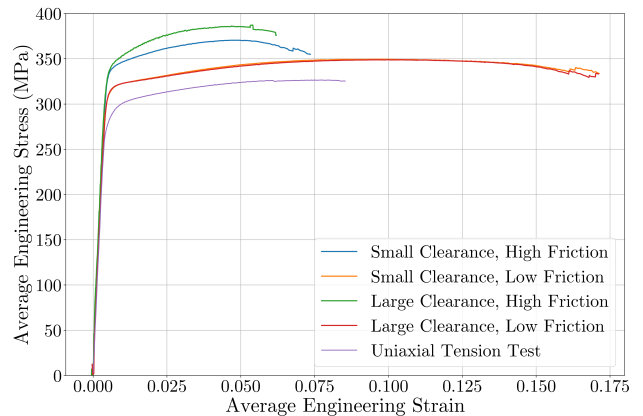
The engineering stress-strain curves for each test in each set were plotted, with an example shown in Figure 21a for Set 4. This allowed the material properties for each test in each set to be obtained and averaged, with the results shown in Table 5. The engineering stress-strain curves for all five tests in each set were then averaged to provide a visual comparison, as shown in Figure 21b.

Table 5: Ring hoop tension test results.

Test	Yield Strength (MPa)	UTS (MPa)	Ductility (%)
Set 1: Dry, Large Clearance	343 ± 3.88	387 ± 11.3	6.21 ± 0.88
Set 2: Dry, Small Clearance	339 ± 2.87	371 ± 3.62	7.36 ± 0.72
Set 3: Lubricated, Large Clearance	318 ± 1.90	349 ± 2.36	17.1 ± 0.67
Set 4: Lubricated, Small Clearance	317 ± 1.91	350 ± 2.45	17.1 ± 0.83



(a) Set 4 engineering stress-strain curves.



(b) Average engineering stress-strain curves.

Figure 21: RHTT engineering stress-strain curves.

The UTT material properties provided a baseline comparison for the RHTT results since they supplied the material input data for the FE model, with a yield strength of 287 MPa, UTS of 328 MPa and ductility of 8.54%. The uniaxial and ring specimens were deemed to have similar properties due to the manufacturing methods that ensured the same grain orientation. However, there may have been a slight variation in the grain size between the centre and outside of the cylinder due to the extrusion strain. The comparison of ductility between the UTTs and RHTTs was less applicable due to different deformation modes. Both the uniaxial and ring specimens experienced a vertical tensile force, where the uniaxial specimens failed in the axial direction, whereas the ring specimens failed in the hoop direction. Additionally, the UTTs had a larger coefficient of variation for ductility of $\pm 16\%$, reducing its reliability as baseline for comparison of ductility with the RHTTs.

Effect of Friction: Set 1 and 2 both consisted of the non-lubricated tests, with a higher FC of around 0.256. Conversely, Set 3 and 4 consisted of the lubricated case, with a lower FC of around 0.0471. Table 3 shows that in the case of a higher FC, the yield strength and UTS were overestimated from the UTTs

to a larger degree compared to that of the lower FC case. Therefore, it was apparent that the presence of friction had a significant effect on the accuracy of strength properties. Whilst the determination of ductility using a RHTT is disputed, it was apparent that the presence of friction caused early failure, as shown clearly in Figure 21b. This implies that with a low FC the ring experienced a more uniform strain distribution. As discussed in literature in Section 3 the presence of a high FC in a RHTT can overestimate the stress properties and, due to early failure, underestimate strain properties/ductility. This is in agreement with the results obtained from these RHTT.

Effect of Clearance: Set 1 and 3 both had a larger clearance of 2.6 mm, whilst set 2 and 4 had a smaller clearance of 1 mm. As stated in Section 3, a smaller clearance is recommended to reduce the bending stresses in the ring specimen. In the case of a high FC (Set 1 and 2), the effect of a larger clearance was apparent as the strength properties had a higher mean, as shown in Table 5. This was also depicted in Figure 21b, where there was an apparent difference between these curves. The larger clearance also caused premature failure, as shown in Table 5 by the smaller ductility in Set 1 than in Set 2. This suggests that a larger clearance overestimates the strength properties and underestimates the ductility in the high friction case. In the case of a lower FC (Set 3 and 4), the effect of the clearance was less apparent. There was a difference of less than 1 MPa in both the yield strength and UTS, which is also shown in Figure 21b where the stress strain curves are similar. This suggested the effect of clearance was not as significant when the setup was lubricated and had a reduced FC.

These results suggested that the key parameter that must be reduced was the FC, this inferred that for a test undertaken with a low FC, the clearance had a minimal effect. The standard deviation of RHTTs was generally lower than that of the UTTs, implying more consistent results.

6.3.2 Capstan Adjustment (DG)

From literature, the stress within the dog-bone is calculated by dividing half the actuator force by the gauge section's cross-sectional area [12]. However, this does not account for the presence of friction and its effect on force distribution uniformity. This force is defined by Equation 14 in Section 5.2. This states that the tensile force experienced by the ring is half the actuator force multiplied by an adjustment factor $e^{-\mu\phi}$, where μ is the FC between the ring and the mandrels and ϕ is the angle along the ring from the horizontal axis. This factor should correct for the presence of friction, which should result in the stress-strain curves for different levels of friction being identical.

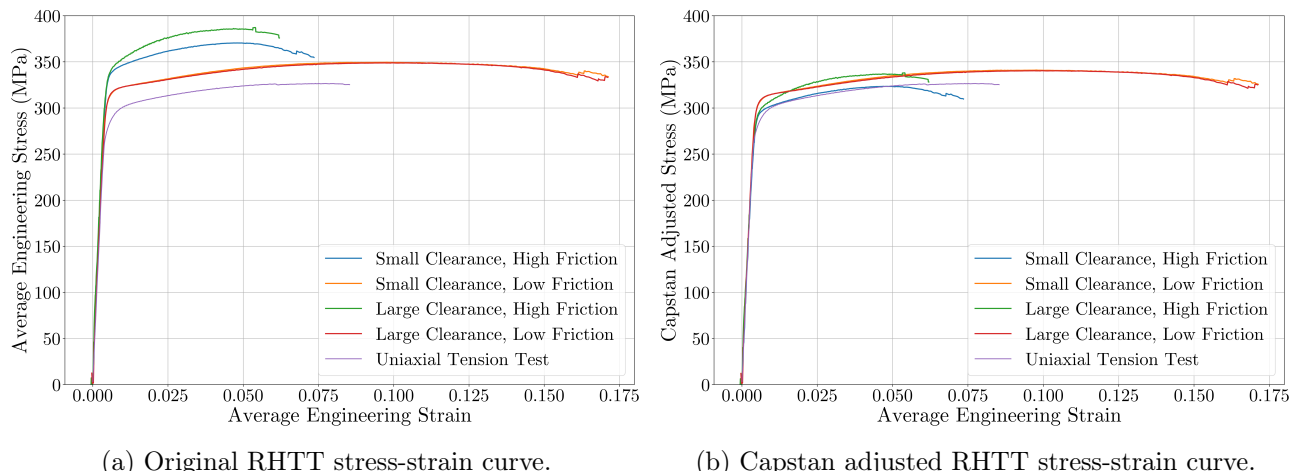


Figure 22: Comparison of the original and Capstan adjusted RHTT stress-strain curves.

In Figures 22a and 22b, the low friction curves became more similar, but were offset from the uniaxial curve. The corrected dry, small clearance curve had the closest match to the uniaxial curve albeit up to 5% ductility, at which point the curve deviated from the uniaxial curve. The Capstan adjustment did not affect the ductility, as it was a factor multiplied by the force and therefore affected the stress, not the strain. The Capstan adjusted material properties are seen in Table 6.

Table 6: Table of the original and Capstan adjusted ring hoop tension test results.

Test	Yield Strength (MPa)	UTS (MPa)	Capstan Adjusted Yield Strength (MPa)	Capstan Adjusted UTS (MPa)
Set 1: Dry, Large Clearance	343 ± 3.88	387 ± 11.3	300 ± 11.0	338 ± 18.3
Set 2: Dry, Small Clearance	339 ± 2.87	371 ± 3.62	297 ± 10.3	325 ± 11.5
Set 3: Lubricated, Large Clearance	318 ± 1.90	349 ± 2.36	310 ± 3.43	341 ± 3.95
Set 4: Lubricated, Small Clearance	317 ± 1.91	350 ± 2.45	309 ± 3.43	341 ± 4.01

From Table 6, the combination of standard deviations from the RHTTs and the friction tests resulted in greater standard deviations for the Capstan adjusted results. It is also apparent that the standard deviations from the Capstan adjusted dry tests increased more compared to the lubricated tests.

6.4 FE Modelling Results (DL, TJC, DG)

This section presents the results from the UTT and RHTT FE models. To validate the models, these results were compared to their experimental counterparts and to the analytical model presented in Section 5, in the case of the RHTT model. The individual effects of varying clearance and friction on the RHTT tensile response are then presented.

6.4.1 UTT Modelling (TJC)

The tensile curve extracted from the UTT model using the method specified in Section 4.4 is presented in Figure 23. The curve demonstrates a strong alignment between the experimental and FEA results. The apparent strength values are shown in Table 7 and indicate strong agreement for the UTS with a deviation of only 0.04%. However, there was a greater discrepancy observed in the yield strength, with a percentage error of 3.10%. This can also be seen in the graph, where the curves diverged around the yield point. At the end of the graph, the engineering stress began to decrease rapidly, so the model could not be used to infer the stress strain behaviour beyond this point. However, the overall strong alignment provided validation that the input material data was accurate and confirmed that FE modelling can replicate simple tension tests with high fidelity.

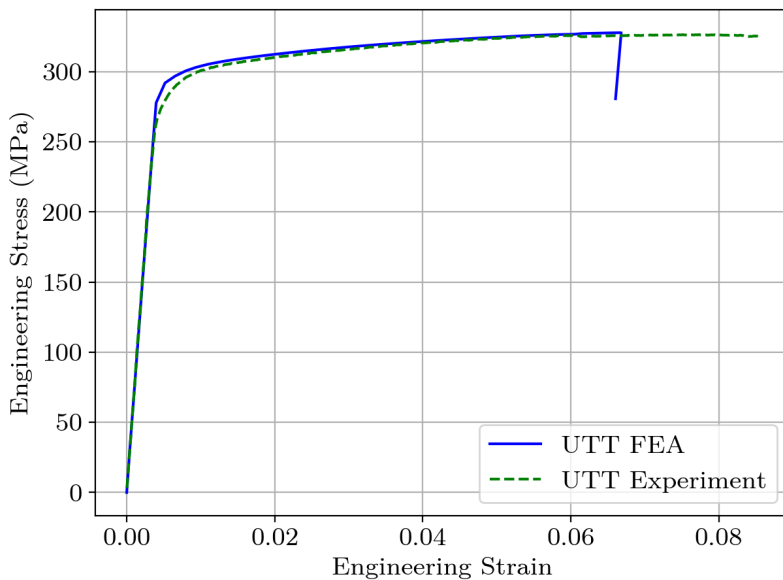


Figure 23: Comparison of UTT FEA results and UTT experimental results.

Table 7: Comparison of experimental and FE model results for yield strength and UTS.

Property	Experiment (MPa)	FE (MPa)	Error (%)
Yield Strength	287	296	3.10
UTS	328	327	-0.04

The stress concentration along the gauge region observed in the UTT FE model was uniform. As discussed in Section 7.1, the specimens fractured at random locations in the five UTTs, which is consistent with this uniformity. This further validated that FE modelling can be used to accurately simulate tension tests.

6.4.2 Validation of the RHTT Model (DL, DG)

This section details the validation of the RHTT FE model through comparison with analytical predictions and experimental results.

Comparison of stress distributions: The trend in stress distribution with increasing an FC predicted by the analytical model detailed in Section 5 is shown in Figure 24.

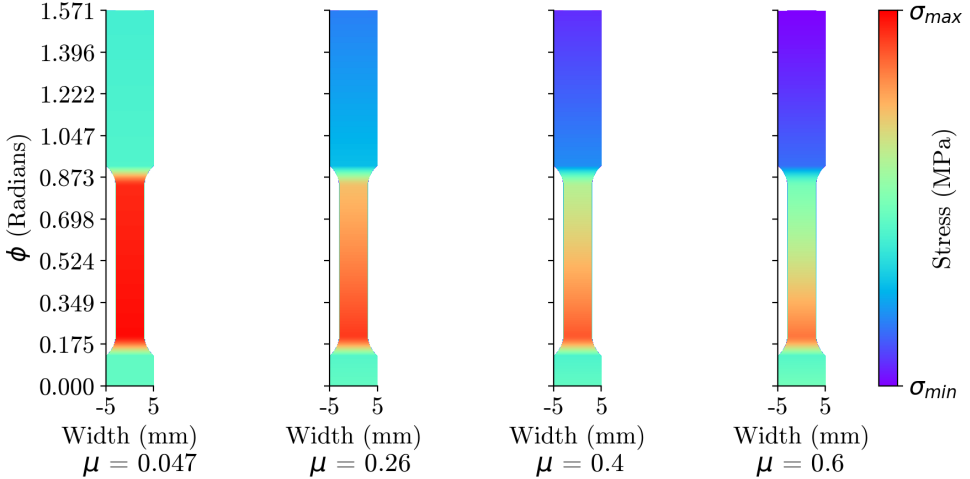


Figure 24: Relative stress distribution map across the dog-bone oriented at $\phi_d = \frac{\pi}{6}$ with varying friction, as predicted by the analytical model.

The analytical model predicted that the maximum stress in the ring was within the dog-bone region due to its reduced cross-sectional area. With no friction ($\mu = 0$), the stress distribution across the dog-bone region was predicted to be uniform, as the exponential term $e^{-\mu\phi} = 1$. The model also showed that as the FC increased, the stress distribution became increasingly localised towards the bottom of the dog-bone, indicating a higher probability of fracture at that location. Therefore, at very low FCs, fracture would occur randomly within the dog-bone region, similar to the behaviour occurring in the uniaxial specimens, albeit with a small tendency towards the bottom. This was also reflected throughout the RHTTs, as mentioned in Section 7.3.1.

A RHTT model was simulated with increasing levels of friction to compare the results in Figure 24, and the results are summarised in Figure 25. The trends in overall stress distribution shape shown in Figures 24 and 25 were well aligned. With an increasing FC, a similar shift from uniformity to lower dog-bone localisation can be observed in these FE results. This is also consistent with experimental findings, since RHTTs performed under dry friction displayed a greater tendency to fracture lower on the dog-bone, with notably greater predictability compared to with lubricated setups. The alignment of numerically and analytically obtained stress concentrations, along with their consistency with the experimentally observed fracture locations, provided strong confidence that the FE model captured frictional effects well, and that the experimental procedure was implemented correctly.

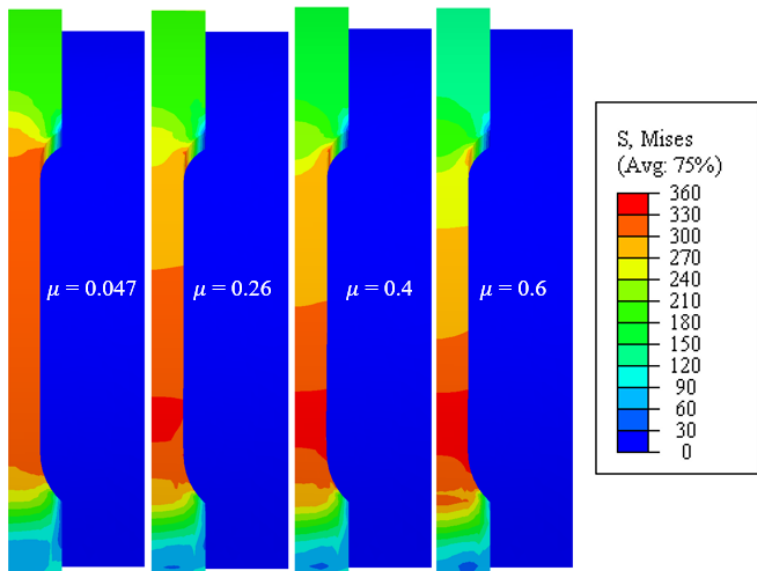


Figure 25: FE-predicted dog-bone stress distributions (MPa) at different friction coefficients.

Comparison with experimental tensile curves: From the RHTT FE model, simulations were run to emulate the four experimental test sets described in Section 4.3, enabling direct comparison of experimentally and numerically obtained tensile curves. The average measured FCs of 0.047 and 0.26 for the lubricated and dry cases respectively were implemented into the models. The 1 mm and 2.6 mm clearances were used, following the experimental procedure. The 1 mm and 2.6 mm clearance models were achieved through use of 50 mm and 49.2 mm diameter mandrels respectively, whilst the FC was set within the interaction module. The resulting four simulated tensile responses are shown in comparison with their averaged experimental counterparts in Figure 26, with dashed lines representing FE results and solid lines representing experimental results. Table 8 summarises the apparent yield strength and UTS from each curve.

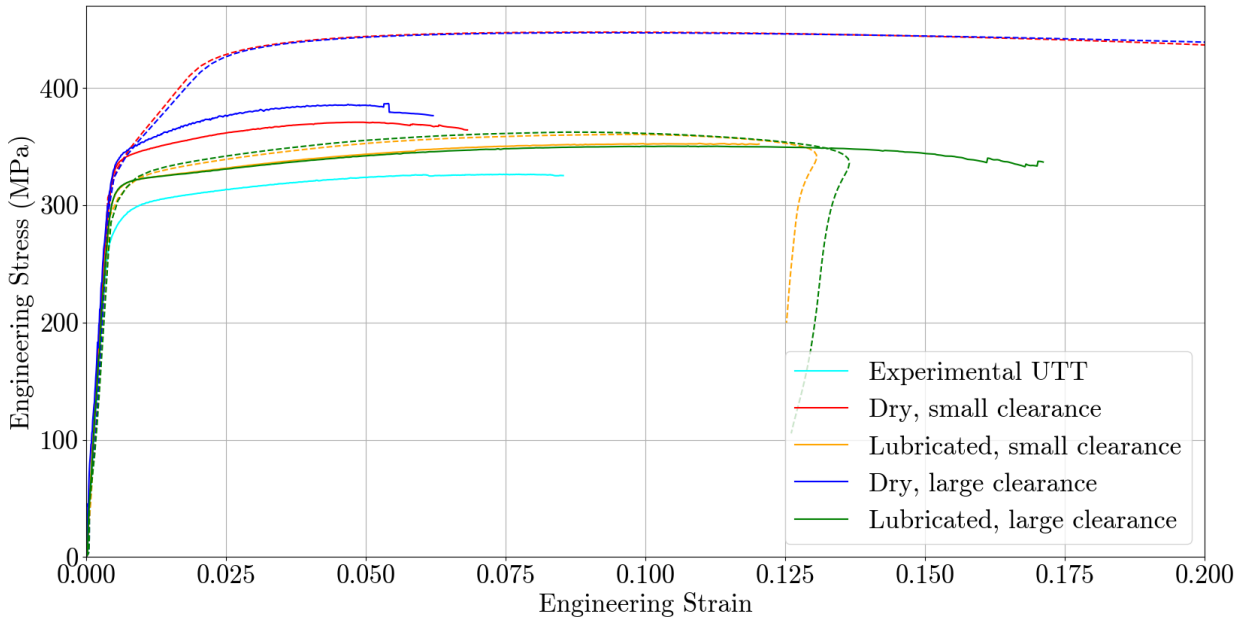


Figure 26: Comparison of numerically (dashed) and experimentally (solid) obtained tensile curves.

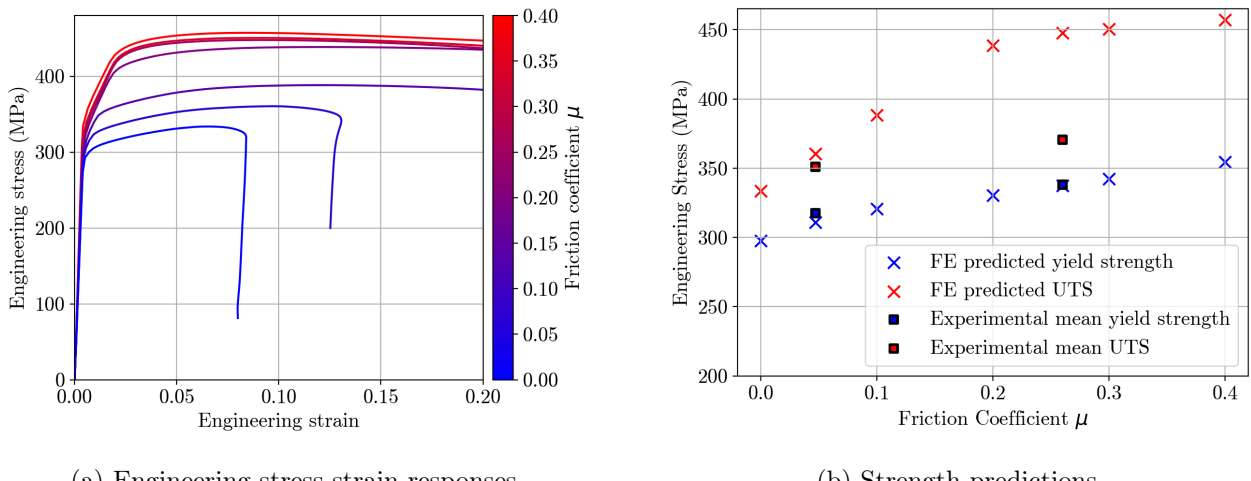
Table 8: FE strength estimates and their error from experimental results.

Set no.	FC	Clearance (mm)	Yield strength (MPa)	Error (%)	UTS (MPa)	Error (%)
1	0.26	2.6	340	-0.59	447	15.78
2	0.26	1	337	-0.25	448	20.85
3	0.047	2.6	314	-0.55	362	3.89
4	0.047	1	311	-1.49	361	2.67

Given the nature of the FE model as a plasticity model which lacked damage characterisation, the prediction of accurate failure and necking behaviour was not possible. As such, it was not appropriate to compare apparent FE ductility estimates to those found experimentally, and so the apparent necking regions shown in Figure 26 were consequently ignored. The apparent necking was instead the result of geometrical instability necking, which was caused by the cross section reduction rate exceeding that of material hardening. The results suggested that the FE model was more accurate at approximating tensile response under low friction, and struggled with accurately predicting results for higher friction conditions. Accuracy also falls at higher strains, leading to an increased error in UTS predictions, which were overestimated for all four cases. In contrast, as shown in Table 8, predictions of yield strength are generally more accurate, though this was slightly underestimated by the FE model for all scenarios. Figure 26 also suggested that the predicted behaviour and thus tensile properties were influenced significantly more by friction level than by ring-mandrel clearance. It was evident that the difference within curves for the same friction level was minimal compared to within pairs of curves for the same clearance level. This was in agreement with findings within Section 6.3, which provided confidence that this effect had been well captured and thus validated the model. It was clear from Figure 26 that in the plastic region, the gradients of the high friction curves differed far more from their experimental counterparts compared to the low-friction curves, which appeared to follow the experimental gradients well. This suggested that the model struggled to predict hardening behaviour under higher friction, resulting in the previously mentioned significant inaccuracies in UTS prediction.

6.4.3 The Influence of Friction (DL)

The impact of increasing friction was further investigated within the FE model, beyond the experimental lubricated and dry friction levels. A clearance of 1 mm was maintained to isolate the influence of friction on apparent tensile behavior. This value was selected as minimal clearance is recommended in the literature, as stated in Section 3.2.2. The FC was varied incrementally between 0-0.4 within the Abaqus/CAE interaction module. The associated tensile responses are plotted within Figure 27a, with extracted strength estimates compared to their experimentally obtained equivalents in Figure 27b.



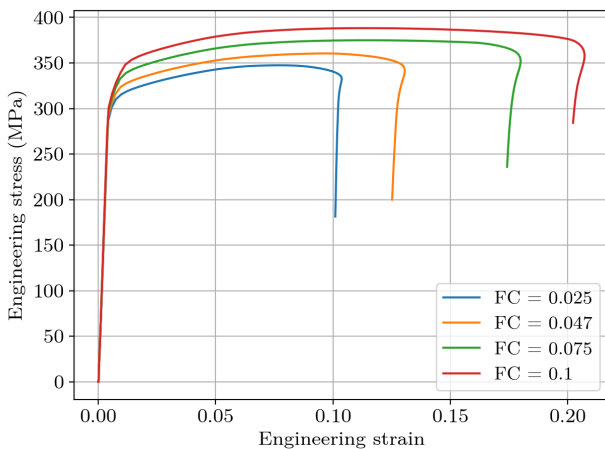
(a) Engineering stress-strain responses.

(b) Strength predictions.

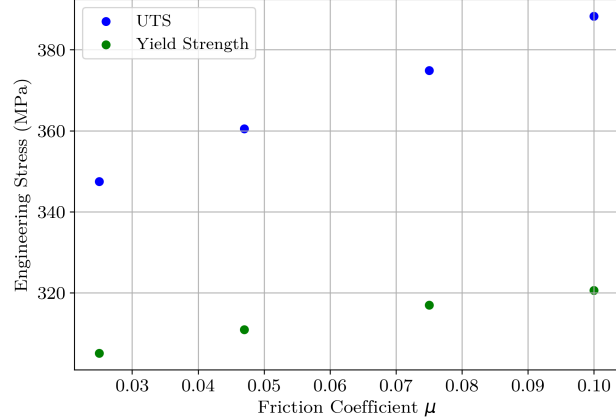
Figure 27: Comparison of engineering stress-strain responses for varying friction levels.

Figure 27a showed that increasing the FC caused inflation of both the apparent yield and UTS relative to their experimental values. As found in Section 6.4.2, Figure 27b also suggested that FE yield strength predictions were relatively accurate compared to their experimental counterparts.

This provided confidence that the rest of the predicted yield strengths are accurate for their respective friction levels, though further experimental results found for greater levels of friction would be necessary to verify this. It was seen that, unlike the trend in yield strength, FE predictions of UTS at higher friction levels were far less accurate due to the aforementioned overestimation of material strength and reduction in accuracy at higher strain levels. To further explore the impact of friction in the experiments, sensitivity testing was conducted. It was necessary to evaluate how critical it was for the FC to be precise as it was difficult to maintain consistent FCs. The FCs of 0.025, 0.047, 0.075 and 0.1 were assessed, as previous findings in Section 6.3.1 indicated that low FCs provided the optimal setup. Additionally, Section 6.4.2 noted that FE modelling provided more accurate predictions of material properties at low friction levels. Figure 28a presents the resulting stress-strain curves, which showed a disparity in the material properties caused by small changes in friction. Figure 28b shows the variation in yield strength and UTS with changing FCs. An increase in friction from 0.025 to 0.047 resulted in a 1.9% increase in yield strength and a 3.76% increase in UTS. Given the inherent difficulty in measuring and controlling FCs, especially at lower levels, these differences could be significant when assessing the accuracy of material properties.



(a) Friction sensitivity tensile curves.



(b) Material properties with varying friction levels.

Figure 28: Results of friction sensitivity study

6.4.4 The Influence of Clearance (TJC)

Clearance was the second parameter investigated in this study. Both literature and experimental testing indicated that larger clearances influence the test results due to bending stresses. To further explore its impact, the FE model was used to analyse the effect of clearance on various material properties. Although there was a greater impact on clearance with higher FC, it was decided to investigate clearance using a low FC as the experimental results shown in Section 6.3.1 indicated that a lower FC aligned more closely with uniaxial test data.

A total of 8 different clearances were assessed, ranging from 0 mm to 5 mm, and including 1 mm and 2.6 mm clearances, which were critical as they matched the experimental clearances. It was decided to keep the ring diameter constant and modify the mandrel diameter instead to achieve these clearances, aligning with the experimental setup. An FC of 0.047 was selected as this was the lowest FC used in the experiments. A step time of 1300 s was used, as this ensured that even for the largest clearance of 5 mm, the simulation ran long enough for the ring to deform past the UTS point. The stress-strain response is shown in Figure 29, while Figure 30 focuses on the elastic and plastic regions.

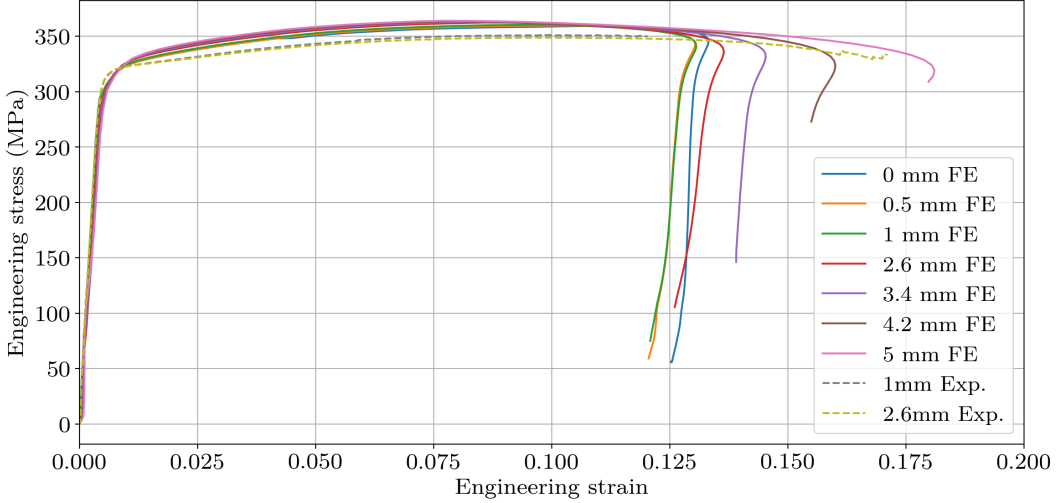


Figure 29: Engineering stress-strain curves for varying clearances.

The data indicated that increasing ring-mandrel clearance led to a higher overall stress. At the start of the elastic region, minor fluctuations were observed in the stress strain curves of larger clearances as seen in Figure 30a. This was likely due to the ring specimen adjusting and settling into position against the mandrel. Additionally, the larger clearance models exhibited a slightly lower gradient in the elastic region, which may indicate an apparent decrease in Young's Modulus. The main discrepancy between the experimental and FE results is that the FE results rapidly decreased in stress at a certain strain, whereas the experimental results continued to increase in strain until failure.

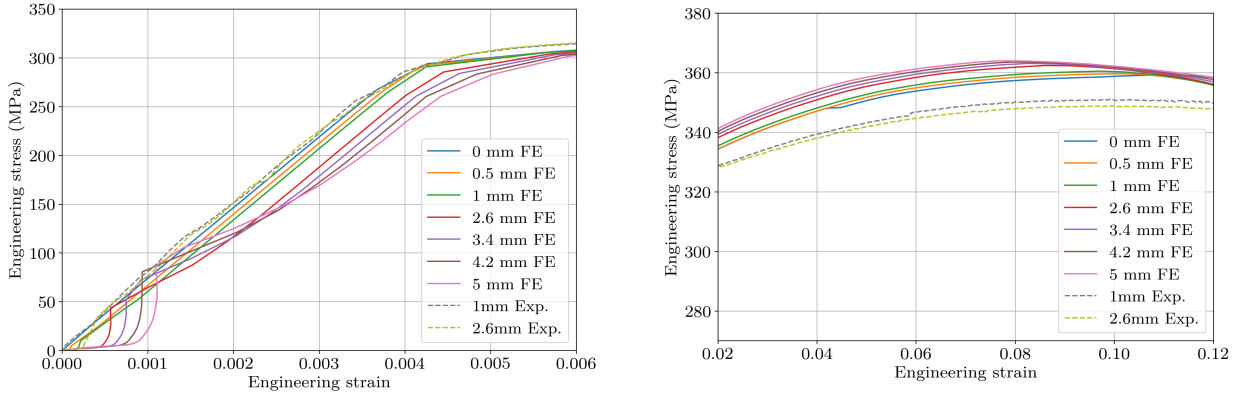


Figure 30: Stress-Strain Curves for varying clearance levels

Figure 31 illustrates the variation of yield strength and UTS with clearance. These are compared against experimental data to evaluate the accuracy of the FE results and identify any underlying trends. The UTS appeared to gradually increase with clearance, following what the stress-strain curve depicts. However, this differed from the experimental results which showed a slight decrease in the UTS with increased clearance. The trend for yield strength from the FE results was also to increase with larger clearances in line with the experimental data. The yield point was determined using the 0.2% offset method. In contrast to the UTT results, there was a greater error between the experimental and FE results for UTS than the yield strength or the low friction results as seen in Table 8.

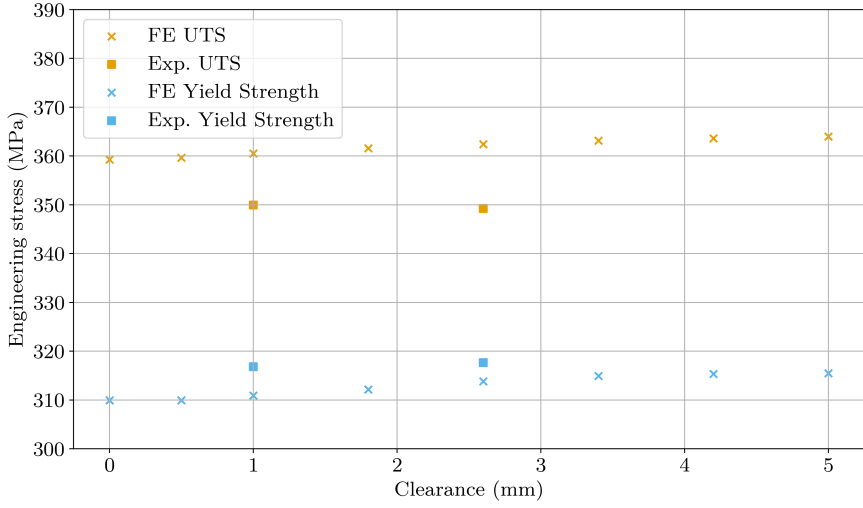


Figure 31: Material properties against clearance for FE and experimental results.

7 Discussion

7.1 Uniaxial Testing (DG)

The experimentally measured value of Young's modulus was 70 GPa, consistent with reported values for a 2 mm plate of Aluminium 6082 T6 [30]. The yield strength 287 MPa and UTS of 328 MPa respectively, also satisfied the expected minimum values of 250 MPa and 290 MPa respectively [33]. However, the ductility had a high coefficient of variation, indicating that there may have been material inhomogeneity that could have led to premature failure. This was especially prevalent in Test 3, where the ductility was significantly lower compared to the other tests. Omitting Test 3 as an anomaly would result in an average ductility of $9.15\% \pm 0.71\%$, and a coefficient of variation of $\pm 7.76\%$, compared to $\pm 16.04\%$ with no omission. However, this reduced coefficient of variation remained relatively large, which suggested the microstructure across the UTT specimens may not have been sufficiently consistent. This was based on a data set with a small sample size of five tests, and therefore it was not possible to determine Test 3 to be anomalous. Therefore, more testing with a larger set of specimens would be required to infer more meaningful statistical significance. Additionally, the fracture locations of the uniaxial samples were randomly distributed across the dog-bone region. This indicated that the stress was uniformly distributed throughout the dog-bone region of the sample.

7.2 Linear Friction Testing (SC, WL)

The investigation aimed to quantify the interface friction coefficients for different lubrication options, with the findings and methods analysed in the following sections.

7.2.1 Evaluation of Results (WL)

From the experimental data, periodic saw-tooth patterns were observed in the time-series as a result of the system undergoing stick-slip transitions. This behaviour was exhibited with greater severity and time-localised standard deviation in the dry and single layer tests. The use of SG increased both the average FC and its standard deviation between tests, whilst tests using only PTFE affected only the standard deviation. For SG, the high viscosity introduced a viscous drag component, which led to a greater opposing force and resulted in greater energy release as the interfaces slip. Variations in SG film thickness may have introduced inconsistencies in test conditions, as the fluid behaved differently between surfaces despite a constant actuator velocity. As a result, wavelet and frequency analysis had broader spectral bandwidths. This also occurred with the 2-layer option since the steel sample exhibited this behaviour when it interacted with the SG. With PTFE, the key irregularities were as a result of physical interactions with the steel specimen in the horizontal load rig. These included the PTFE tape

dragging or compressing in front of the moving steel block. As this behaviour was unpredictable, the actuator load standard deviation increased with the work that was required to deform and displace varying amounts of PTFE across tests. From Table 4, the higher maximum amplitude coefficient was due to the increased layer thickness as a result of the PTFE. This led to a higher effective normal force between the friction interfaces as the PTFE tape conformed to surface asperities on the metal, acting as an adhesive and causing more severe slip amplitudes. For these reasons, PTFE test results were measured to have a higher FC and standard deviation, reducing its reliability for RHTT testing.

Using single layers, the results showed high variances within and across tests, while both multiple layer configurations proved effective in improving all measures. As stated in Section 6.2, it was found that the 2-layer reverse option had the lowest FC of 0.0471, which was therefore used in the RHTT experiments. This was due to the combination of multiple layers creating a more standardised surface condition; the PTFE may have acted as a constraining surface to maintain a consistent SG film and prevented localised dry patches, which caused the system to remain in traction and act within a single lubrication regime. Conversely, the SG may have contributed towards lubricating the PTFE interface, which lowered the potential for dragging and acted as a viscous damper for slip events.

7.2.2 Setbacks of LFT (WL)

A new rod was manufactured to have a slide fit, in order to reduce the friction within the LFT setup, as discussed in Section 4.2.1. However, it remained possible that some residual systematic error could have remained.

For configurations involving SG, the film thickness was not standardised. Future tests should be performed using coating bars or film applicators to ensure this variable is controlled. As shear stress varies with shear rate, tests should be performed using different actuator velocities to obtain a representative FC distribution. Additionally, configurations using PTFE tape should ensure consistent tension when prepared over the aluminium specimen, as this can affect the interaction behaviour between the PTFE tape and steel specimen in the horizontal rig.

As mentioned in Section 4.2, the actuator force was initially set to 250 N, using a screw to fix the horizontal specimen attachment to the rig. However, the load cell recording progressively became more negative throughout all tests, indicating a consistent error. While general linear friction tests may be subject to system creep or high speed non-linearities, this is unlikely given the magnitude and speed of forces used. A more probable source of error was due to mechanical relaxation of the screw as it was only fixed at the start of a test. Additionally, as the specimen was not fixed to the actuator, there was a slight misalignment in the horizontal rig. This caused an additional moment to be created as the steel block was not completely parallel with the contact surface, resulting in an artificially introduced normal force. To account for this, a linear interpolation was used to capture the behaviour of the horizontal force, as detailed in Section 4.2.2. However, the assumption of a linear normal force may not have been entirely appropriate to capture minute deviations in the normal force applied. For future testing, a more accurate metric should record this to the same frequency resolution as the actuator force.

7.2.3 Considerations for Comparison of FCs between the LFT and RHTT (SC)

The LFT was used to quantify the FCs for the various lubrication options, with the best selected for use in the RHTT and subsequently the FE model. The FCs obtained from the LFT provided a range for each lubrication option. For the dry condition, the range was 0.226-0.284, whereas the 2-layer reverse lubrication had a more consistent mean FC, with a range of 0.0349-0.0613, which was notably smaller than the dry range. These ranges introduced greater variation in the FCs in the actual RHTT. Since both the dry and 2-layer reverse were used in the RHTT, the mean FC for each was applied as a constant in the FE model. However, this introduced limitations in comparing the FE results to experimental outcomes, as discussed in Section 7.4.3, since the FC in the RHTT was considered within a range rather than a fixed value. Additionally, there could be slight discrepancies between the FCs measured in the LFT and those in the RHTT due to the differences in the test geometries, where the

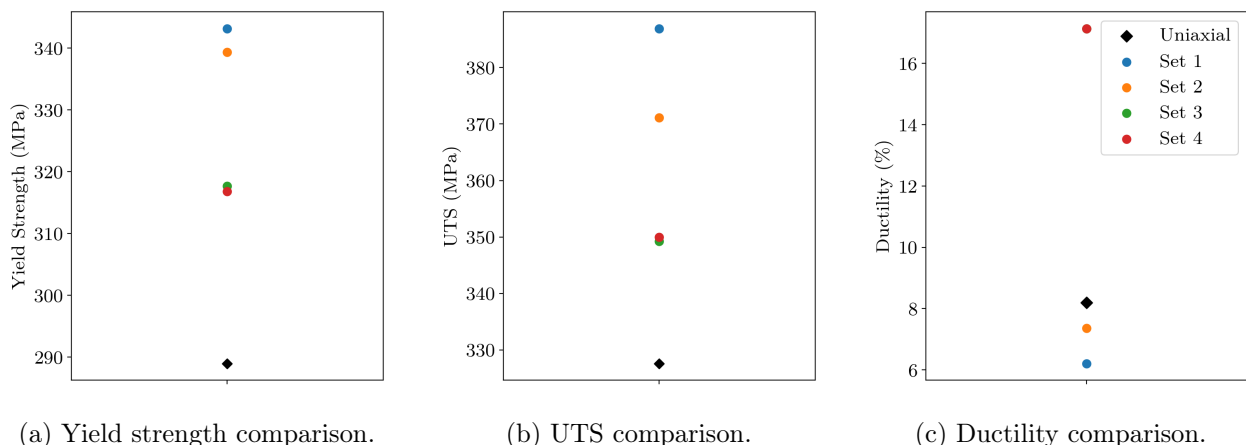
RHTT is bi-directional whereas the LFT is unidirectional. The differences in the testing configurations could have led to a slight variation in the FC between the two tests.

7.3 Ring Hoop Tension Test (SC, DG)

The investigation into the RHTT aimed to evaluate the key parameters influencing the accuracy of material property determination in the hoop direction. The findings were analysed in order to provide recommendations for a procedure to determine material properties of metal spun components for GKN Aerospace.

7.3.1 Evaluation of Results (SC)

As discussed in Section 6.3, the presence of a high FC had a greater influence on the accuracy of the material properties determined than the effect of a larger clearance. The effect of clearance was also found to be minimal in the lubricated case with a lower FC. The RHTT results mostly had a reduced standard deviation for the yield strength, UTS, and ductility, compared to the UTT results. This implied more consistent and reliable results were obtained using the RHTTs. Figure 32 shows the material properties of the RHTT test sets compared to the uniaxial data. Ductility is heavily influenced by the testing methods since it is largely instability based during necking. The ductility, shown in Figure 32c, was determined to be less comparable to the baseline results of the UTT due to different deformation modes being experienced by the samples in the UTTs and the RHTTs.



(a) Yield strength comparison. (b) UTS comparison. (c) Ductility comparison.

Figure 32: Material properties for each set of tests in the RHTT.

Friction:

As discussed in Section 6.3 it was apparent that the FC had a significant effect on the accuracy of material property determination. In this investigation, the dry case exhibited a mean FC of 0.26, although this value likely varied within the range observed in the LFT. The lubricated case, which consisted of SG next to the aluminium ring sample and PTFE tape layered on top, reduced the FC to 0.047. Therefore, the lubricated option FC was below the threshold of 0.1 recommended by Dick et al. for hemispherical mandrels [12]. The FC range for this lubricated case was considerably less than that of the non-lubricated case, inferring greater consistency and making it more suitable for comparison with the FE model.

The fracture region for the uniaxial specimens was observed at varying locations across the dog-bone region. In the non-lubricated case for ring specimens, fracture was consistently located near the bottom of the dog-bone region. This observation supported the localised stress concentrations predicted by the analytical model and FE models, as presented in Section 6.4.2, under conditions of higher friction. Conversely, in the lubricated case fractures were observed at different locations across the dog-bone region. This behaviour mirrored that of the UTTs, and also aligned with the stress concentrations predicted for low FC conditions in the analytical and FE models.

The application of lubrication, which reduced the FC, resulted in a decrease in the contact stresses between the mandrel and the ring. This reduction in contact stresses helped to minimise localised strain concentrations, delaying the onset of necking and crack formation that is typically induced by high friction. This was apparent with the increased ductility for the lubricated sets, which exhibited an average increase of 10.3% in ductility compared to the non-lubricated specimens. The material underwent more uniform deformation with a low FC, which enabled a more accurate determination of the material's stress-strain behaviour. A decrease in average yield strength of 24 MPa and UTS of 29 MPa was observed from the non-lubricated sets to lubricated sets. When using the UTT results as a baseline, for the small clearance, this was equivalent to a 18.1% error in the non-lubricated case and 10.5% error in the lubricated case for the yield strength. For the UTS there was a 13.1% error in the non-lubricated and a 6.7% error in the lubricated set. The small clearance results were used for this comparison since in literature it is recommended that a smaller clearance leads to more accurate material properties determination. Therefore, the lubricated values provided material properties that were more consistent with those obtained in the UTT results. This shows the significant inaccuracies in the material properties determined when inadequate lubrication was used. The use of lubrication also reduced the standard deviations in the yield strength and UTS. This implied more consistent and reliable results will be determined when using sufficient lubrication.

The reduction in FC minimised excessive frictional forces, providing experimental measurements that were closer to the true material properties. Whilst this was a crucial factor in the RHTT, it is likely that in practical application, the use of lubrication to reduce the FC would be a common practice to ensure accurate material property determination. In accordance with established literature, it is recommended that all RHTTs are conducted with the lowest feasible FC to ensure reliable results.

Clearance:

In this investigation, the clearance was found to have an effect with a high FC, but this was minimal when a low FC was applied. The two clearance levels tested were a smaller clearance of 1 mm and a larger clearance of 2.6 mm.

The influence of clearance was more apparent in the dry case. Although the initial clearance was removed before starting the experiment, bending stresses occurred along the sides of the ring specimen in the gap between the mandrels during the test. This effect was particularly evident in the larger clearance case, where a greater lateral deformation caused greater bending stresses along the sides of the ring specimen. These bending stresses contributed to localised high stress concentrations, which restricted the overall elongation of the ring. This caused an overestimation of the yield strength and UTS, and an underestimation of ductility. This was demonstrated by a decrease in average yield strength of 2.3 MPa and UTS of 7.6 MPa from the large to the small clearance sets. Conversely, the ductility increased by an average of 0.6%, when moving from larger clearance to the smaller clearance. This demonstrated a slight change in the material property determination; however, this average primarily accounted for the difference in clearance in the non-lubricated scenario. This is apparent in Figure 32. When the friction was sufficiently reduced, the influence of clearance significantly decreased. This was apparent in the results where the difference in clearance for the lubricated cases had a difference of 1 MPa for the strength properties and had the same ductility. This was also apparent with the percentage error from the UTTs for the lubricated tests where the large clearance had a 10.8% error and the small clearance had a 10.5% error for the yield strength. This showed the effect was minimal since there was a difference in error of 0.3%. Therefore, a lower FC resulted in a more uniform stress distribution across the ring during the test, as the frictional forces were minimised, this could infer the bending stresses were also minimised.

With a high FC, the standard deviation was found to decrease significantly in the UTS from 11.3 MPa for the large clearance to 3.62 MPa for the small clearance. The standard deviations also reduced for the yield strength and ductility, from the large clearance to the small clearance sets, albeit with a modest reduction. However, in the lubricated sets there was no trend observed, since there was a minimal difference in the standard deviations between the clearance levels.

Although smaller clearances reduced bending stresses, leading to more accurate material property

determination, the effect of clearance became less critical when the FC was reduced. This was due to friction serving a more significant role in controlling the accuracy of the test results. Additionally, since material property determination using a RHTT would typically occur with low friction, the impact of clearance becomes less significant. Furthermore, controlling the FC is more manageable than controlling the clearance, especially considering the potential variations in diameter of a ring specimen from a metal spun component. Therefore, friction is the most important factor to control to ensure accurate material property determination.

It is recommended to reduce the clearance where possible. However, since it was found that with a low FC a clearance of 2.6 mm did not adversely affect the results, reducing the clearance is not as important as keeping a low FC. Additionally, smaller clearances reduce the ability to apply lubrication effectively. Therefore, the clearance should be sufficient to allow for application of lubrication, ensuring that friction is minimised to maintain the accuracy of the RHTT.

Setbacks of RHTT Setup:

The DIC enabled measurements of 3D displacements of the dog-bone region by recording the specimen in a 3D space along its curvature. Whilst this method was effective, it had certain limitations. The DIC relies on speckled paint to track movements from a distance. However, during necking the speckled paint fractured, which potentially led to data reduction and inaccurate measurements near failure [12]. Furthermore, recalibrations were not performed before each test. This was considered acceptable as the top actuator of the INSTRON 1341 remained in a fixed position throughout the testing, ensuring the top mandrel and dog-bone region remained consistent for each test. However, if testing were to occur over a longer time period, it would be sensible to recalibrate before each test set.

7.3.2 Capstan Adjustment (DG)

One limitation of the analytical model was that the effect of strain was ignored, as it assumed the ring was in constant contact with the mandrels. However, in the experiments at high friction the stress distribution across the dog-bone was found to be non-uniform, which meant that the strain was also non-uniform. Therefore, the angle of the dog-bone changed throughout a test, which was not considered in the Capstan adjustment factor. This meant that the analytical model behaved as an instantaneous stress model, so it was more accurate for low values of strain.

The Capstan adjusted curves were more in line with the UTT results, as detailed in Section 6.3.2, although they did not align as well as expected. This showed the Capstan adjustment factor only partially captured the stress behaviour in the ring specimens. As discussed in Section 5.1, the analytical model negated the effect of bending due to clearance, as the ring curvature was largely unchanged throughout each test. The effect of clearance was not corrected for in the Capstan adjusted curves. This was apparent in Figure 22, for the high friction cases, where the larger clearance curve remained at a higher stress than the smaller clearance curve. Therefore, to achieve a more accurate adjustment factor, the shear force and resulting bending moment should have been considered. However, this would only have been possible for the section of the ring in contact with the mandrels. This is because the force acting in the gap zone are only the tensile force straightening the dog-bone and the resulting shear force and bending moment. However, it is impossible to relate these forces as they are orthogonal to each other. A solution to this would be to apply the Capstan adjustment factor incrementally throughout each test, as the dog-bone angle changes.

Another source of inaccuracy was the value of the FC input into the model, as was detailed in Section 7.3.1. Since the FC was obtained experimentally, any error in its value was carried over into the Capstan adjustment factor. This was reflected in the standard deviations of the Capstan adjusted RHTT results, which incorporated both the standard deviation for the RHTT results and for the LFT results. This meant the standard deviation for the Capstan adjusted results were greater than the original results, especially for the dry tests due to the larger wavelets, as detailed in Section 6.2. Due to this, the Capstan adjustment factor may have over-corrected the dry stress-strain curves, as the effect of bending was not considered.

7.4 FE Modelling (DL, TJC, DG)

This section provides a critical analysis of the FE model results for the UTT, RHTT, and friction and clearance investigations. It aims to evaluate the accuracy and validity of the simulations by comparing them with experimental data and the analytical model.

7.4.1 RHTT Analytical Stress Model Limitations (DG)

The analytical and FE models disagreed regarding the trend in maximum stress with an increasing FC. The analytical model suggested the maximum stress decreased with an increasing FC, whereas the FE model showed the opposite. Despite this, the overall trend in stress distribution predicted by the analytical model was similar to that of the FE model as discussed in Section 6.4.2. In both models, as the FC increased, the stress became more concentrated towards the bottom of the dog-bone. This trend is more significant in the context of capturing the frictional effects in the RHTT FE model.

7.4.2 UTT FE Modelling (TJC)

As discussed in Section 6.4.1, the UTT FE results aligned well with the experimental data. This was as expected since the plastic region material data was derived from an extrapolation of the average experimental UTT stress-strain curve. However, there was a larger error observed in the yield strength compared to the UTS. This can be seen in Figure 23, where the curves diverge at the yield point. One reason for this difference is the way in which the material data was input into the model. Since only plastic data was entered, the elastic region was only defined by the Young's Modulus. This resulted in an undefined elastic-plastic transition zone, which may have contributed to the greater error in yield strength.

Another notable discrepancy between the experimental and FE results was observed at the end of the stress-strain response. In the FE results, a rapid decrease in stress occurred at a strain of approximately 0.067, indicating that the simulation became unreliable beyond this point. This differed from the experimental results, which continued up to the point of fracture at a strain of around 0.085. This drop potentially occurred because of extreme node distortion due to necking, as detailed in Section 6.4.2. Despite this divergence, the FE results remained valid up to the yield and UTS points, which are the key material properties investigated in this study. Since ductility was not a main focus of the FE investigation, as explained in Section 4.4, the model's inability to capture the stress-strain behaviour beyond this point did not significantly impact the outcomes of this study.

7.4.3 RHTT FE Modelling (DL, TJC)

The apparent failure points seen on various curves in Section 6.4.2 were ignored for the analysis of results. This apparent necking within the RHTT model only considered geometrical instability necking, which arose purely due to the cross-sectional area reduction rate exceeding the hardening rate of the material. Since the FE models lack a damage criterion, damage-induced necking was disregarded. As such, necking and therefore ductility predictions from the FE models were not accurate. However, given the variability in ductility observed between UTT and RHTT experimental results, and as the RHTT experimental ductility was only an indication of the material's actual ductility, achieving precise ductility measurements from the RHTT method was not a primary focus.

The results of the friction study in Section 6.4.3 further supported that the model accuracy decreased with greater friction levels through increasingly significant overestimations of strength properties. This difference in accuracy between the two friction levels was due to the greater uncertainty in FC measurements for the dry case than for the lubricated case, as discussed in Section 7.2.3. This led to a much less accurate average FC measurement for the dry case, which was then input to the Abaqus/CAE model. As such, the resulting FE tensile curves may not have been directly comparable to their experimental counterparts. This offered a plausible explanation for the differences in apparent FE modelling prediction accuracy.

The friction sensitivity study demonstrated the need for consistent lubrication application to ensure the FCs remain as expected. This study showed that relatively small variations in the FC can lead to changes in the accuracy of material property determination, in line with the larger friction study.

Despite possible issues with the input dry FC, the RHTT FE model still clearly captured the overestimation of material strength with increasing friction that was observed experimentally. As such, the model partially succeeded in capturing the general trend of increasing ring-mandrel friction. Irrespective of the issues with modelling higher friction in the RHTT FE modelling, it remained capable of accurately modelling low friction tensile responses. This was ideal since low friction scenarios were found to be more optimal for measuring tensile responses. One key limitation associated with using FE models to assess the stress-strain response across varying clearance levels was in determining the appropriate simulation step time. Varying clearances required the simulation to run for different time periods before the mandrels and ring specimens made contact and began to deform. A fixed step time of 1300 s was chosen, as it ensured that all clearance levels reached the UTS point. However, for smaller clearances this duration was longer than necessary. Therefore, further investigation is recommended to identify the optimal simulation time for each clearance level. This would reduce unnecessary computation time and potential cost, especially in more complex simulations. The clearance study displayed some fluctuations in the elastic region for higher clearances, which may have been due to the specimens settling into place. This may have distorted any Young's modulus calculations, and further validated that RHTTs are not an accurate method of measuring Young's modulus as discussed in Section 3.1. Furthermore, as yield strength was calculated using this gradient, the calculated yield strength values for higher clearance levels may not have been accurate. Within the clearance investigation at low friction there was a discrepancy between FE and experimental results regarding the UTS trend. In the FE simulation, UTS increased with larger clearances, whereas in the experiment UTS slightly decreased. However, this decrease was minimal, at just 0.7 MPa. Testing a wider range of clearances experimentally could help determine whether this trend is consistent. The clearance study showed that with increasing clearances, the material properties of yield strength and UTS were overestimated when compared to the uniaxial experimental results, aligning with the RHTT experimental trend.

Overall, despite some limitations, the key findings from the FE results remained valid. The results showed that for tests with increased FCs or larger clearances, the material properties would be overestimated in comparison with the UTT results. It also revealed a larger variation between the simulations with different friction levels compared to those with different clearance levels. This indicated that friction has a larger effect on the stress-strain response and material property determination than clearance, in line with the experimental results.

8 Critical Evaluation (All)

The overarching aim of this study was to identify which parameters had the greatest impact on the accuracy of RHTTs. The parameters investigated were friction and clearance. Overall, this aim was successfully met as the findings demonstrated that friction had a greater impact on the determination of key material properties than clearance. This was evident in the experimental results, where a greater variation in the stress-strain curves was observed between different friction levels compared to different clearance levels. The FE results further validated this, as a similar trend was seen with a greater disparity found between simulations with varying FCs than those with differing clearances. However, the level of the investigated parameters necessary to ensure accurate material property determination remains qualitative at this stage. To improve the reliability of the results, further work is necessary to assess the impact of each parameter quantitatively. This would enable the development of standards for RHTTs to specify acceptable parameter limits. For example, by defining the maximum allowable FC or clearance level. The establishment of these standards would assist in supporting companies such as GKN in implementing a validated test method to evaluate material properties in tubular components, as accurately determining material properties is crucial in industries such as aviation.

The first objective was to critically review the literature on the key parameters influencing the accuracy of RHTTs and to propose an optimal testing setup by utilising the current state of the art. This

objective was successfully achieved, as it was determined that friction and clearance are the primary factors affecting the accuracy of the RHTT. Various RHTT parameters and setups were evaluated to identify the most effective configuration, incorporating all feasible state of the art setups. The chosen setup focused on investigating both the clearance and friction levels. However, an even more optimal setup utilising roller needle bearing mandrels could reduce friction further, although this would have limited the ability to easily vary and analyse different friction levels.

The second objective was to use standard tensile tests to determine the material properties for samples that were manufactured to have the same grain orientation as the ring samples. The Young's modulus, yield strength, UTS and ductility were successfully determined for aluminium 6082 T6, which could then be used as a baseline for comparison of the material properties determined from the RHTT. The mean Young's modulus was found to be 70 GPa, which was the same as the expected value, inferring the material properties determined were accurate. Whilst these UTT results provided a good baseline for comparison, these values may not have been the true material properties for the ring specimens. This is due to potential differences in the microstructure.

The third objective was to determine the estimated interface FCs under varying lubrication conditions between aluminium and steel. The FCs for different lubrication levels were successfully quantified using an LFT. However, the results found provided a range of FCs, with the dry condition showing a significantly larger range compared to the 2-layer reverse option. This meant that the dry sets used in the RHTT likely exhibited a less consistent FC than the lubricated sets. Additionally, the test configurations of the LFT and RHTT had different geometries and therefore the FCs obtained from the LFT may not be entirely comparable to those in the RHTT.

The fourth objective was to determine the impact of ring-mandrel lubrication on the apparent material properties, using experimental and FE procedures. This was successfully achieved, as it was found that in the RHTT experiments a high FC had a significant impact on the accuracy of the material properties determined. Consequently, it is recommended to focus on the reduction of friction as the primary parameter to optimise accuracy. Whilst this conclusion is useful, the tests did not quantify the specific levels of friction that might negatively impact the accuracy of material property determination. This data would be crucial for establishing standards for RHTTs. In the FE model, friction was also found to have a large impact on the accuracy of material property determination. Even small variations in FC led to noticeable differences in the accuracy of material properties found. However, due to the measured FCs having a large range, it is likely that the FC values input into the FE model did not exactly match the experimental conditions. This would explain the discrepancy between the experimental and FE results.

The fifth objective was to utilise experimental and FE modelling methods to evaluate the effect of the clearance between the mandrel and sample on the apparent material properties. This was successfully achieved as it was found that the level of clearance only significantly affected the accuracy of the material properties determined under high friction. However, only two levels of clearance were experimentally tested, so conclusive trends could not be drawn on the level of clearance that negatively impacts the accuracy of the results. Therefore, to investigate more levels of clearances the FE model was developed. The FE results indicated that clearance had a minimal effect on the accuracy of material property determination, aligning well with the experimental results. A constraint of the FE clearance investigation was the simulation running time, as differences in clearance led to inconsistencies in the duration of the deformation phase following ring-mandrel contact.

8.1 Limitations

The DIC technique proved valuable for obtaining displacement and strain data in a 3D space. This method relied on applying speckled paint on a region of interest to allow for monitoring and data acquisition. However, the speckled paint split as the specimens were pulled apart, which potentially led to data loss near failure. To ensure more reliable results, alternative methods for capturing strain or displacement data could be considered. This could include using a custom strain gauge designed specifically for the ring specimens.

The limited number of specimens that could be manufactured posed a constraint on the evaluation process. This restricted both the number of parameters that could be assessed and the number of specimens tested in each set. Since there were only five specimens per tested set, it was not possible to perform rigorous statistical analysis. Statistical methods are essential for assessing the reliability and variability of the results, and identifying any potential outliers.

Since the FC for higher friction conditions had a greater range of values, the FC entered into the analytical and FE model may not have been accurate. As a result, at higher levels of friction, the Capstan adjustment factor and the FE simulation may not have truly reflected the conditions of the physical experiments. Additionally, the FE model did not incorporate a damage model, so it could not be used to measure ductility. Due to fluctuations in the stress-strain curve at higher clearances, the FE model failed to accurately predict the Young's modulus, which could in turn affect the estimation of the yield strength.

8.2 Future work

A key area for future work would be to test a wider range of friction and clearance levels with greater precision. This should be conducted alongside experiments with larger sample sizes, which would enable more rigorous statistical analysis. This would allow for evaluation of the data distribution, identification of any potential outliers, and assessment of the consistency of results across the different sets. This would provide a more comprehensive understanding of the material's behaviour and increase the robustness of the findings.

More refined testing of friction and clearance, particularly looking at the lower friction levels and smaller clearance levels, would provide a quantitative analysis that establishes clear standards for selecting appropriate friction and clearance levels for different scenarios. Additionally, future studies should include specimens with varying diameters, such as specimens obtained from metal spun components, to assess the effect of these variations' influence on the accuracy of material property determination.

The testing of heat treated aluminium samples in the RHTT would provide a valuable comparison to untreated samples. The heat treatment would alter the material properties, enabling a comparison of results to verify if the RHTT accurately captures the changes in the material properties. This would help to validate the RHTT method's effectiveness in determining material properties accurately.

Further development of the RHTT FE model should primarily focus on incorporating damage characterisation, such as through the Johnson-Cook ductile damage initiation criterion [34]. This enhancement would enable high fidelity representation of material ductility across various test scenarios, allowing for the meaningful evaluation of frictional/clearance effects on ductility. The inclusion of strain-rate-dependent material properties to account for loading speed effects is also a model enhancement that should be considered. Moreover, finer discretisation on ring-mandrel contact surfaces and use of alternate friction models such as the Lagrange multiplier method also hold potential to increase model fidelity. The addition of initial stresses within the model to replicate experimental preloads could also improve the simulation.

The analytical model could be improved further by incorporating the effects of bending stresses. Additionally, the Capstan adjustment factor could have been applied incrementally, due to the changing dog-bone angle throughout each test. This would allow for a more detailed investigation into the effectiveness of the adjustment factor.

9 Conclusion (All)

The use of hydrogen as an alternative fuel source is gaining traction, due to the global initiative to reduce carbon emissions. One of the most common ways to safely store hydrogen, and utilised by industry leaders GKN Aerospace, is in metal spun, dome-shaped pressure vessels. These components are safety critical since failure can result in catastrophic consequences. To ensure their structural integrity it is essential to accurately understand their material properties, particularly in the hoop

direction since this direction is the most susceptible to failure. The RHTT is a non-standard method that could be applied to assess the material's behaviour in the hoop direction.

This investigation used UTTs to effectively determine aluminium's material properties, which were then used as an input for the FE model and served as a baseline comparison for the material properties obtained in the RHTTs. LFTs were performed to quantify the various FCs that could be used in the RHTT. The lowest FC identified was 0.047, from the 2-layer reverse lubrication option. This was then selected for use as the lubricated option in the RHTT.

The RHTTs were conducted with four test sets, each with five ring specimens. These sets varied the friction levels (dry and lubricated) and clearance levels (1 mm and 2.6 mm) to assess the impact of these parameters. The results found that friction had a more significant effect on the accuracy of material property determination than clearance. High FCs overestimated the yield strength and UTS, whilst underestimating the ductility. A larger clearance provided a similar conclusion with a high FC, but this effect was minimal with a lower FC. These findings indicate that controlling friction is critical for accurate material property determination, whilst clearance has a lesser influence.

FE modelling provided reasonable accuracy for predicting tensile responses in the UTT as well as for low friction load cases in the RHTT. The RHTT FE model aligned closely with the experimental results for yield strength, with errors of as little as 0.25%. Conversely, the model significantly overestimated material strength relative to experimental results when used to simulate in higher friction scenarios. Moreover, the FE models were not designed to provide ductility estimates since they lacked a crucial damage model, which would have required a significant additional layer of complexity. For these reasons, the use of the presented RHTT model is only recommended for the emulation of lubricated conditions for strength estimates, and ductility estimates should not be taken from the model, unless damage modelling capabilities are implemented to better predict high strain behaviour. Despite some limitations, the FE model further validated the experimental trend observed, where friction had a greater impact on the accuracy of material properties than clearance.

This investigation established a foundation for the development of standardised procedures for RHTTs to assess material properties. By improving the accuracy of material property determination through methods like RHTTs, the structural integrity of safety critical components can be ensured, supporting the development of safe and reliable hydrogen storage methods for aviation.

References

- [1] F. Nagase, T. SugiYama and T. Fuketa, “Optimized ring tensile test method and hydrogen effect on mechanical properties of zircaloy cladding in hoop direction,” *Journal of Nuclear Science and Technology*, vol. 46, no. 6, pp. 545–552, 2009. DOI: 10.1080/18811248.2007.9711560.
- [2] P. Friedlingstein, M. O’Sullivan, M. W. Jones, R. M. Andrew, J. Hauck, A. Olsen *et al.*, “Global carbon budget 2020,” *Earth System Science Data*, vol. 12, no. 4, pp. 3269–3340, 2020. DOI: 10.5194/essd-12-3269-2020.
- [3] T. Yusaf, A. S. Faisal Mahamude, K. Kadirkama *et al.*, “Sustainable hydrogen energy in aviation – a narrative review,” *International Journal of Hydrogen Energy*, vol. 52, pp. 1026–1045, 2024, ISSN: 0360-3199. DOI: <https://doi.org/10.1016/j.ijhydene.2023.02.086>.
- [4] P. Sharma, S. Sharma, T. Bera *et al.*, “Effects of dome shape on burst and weight performance of a type-3 composite pressure vessel for storage of compressed hydrogen,” *Composite Structures*, vol. 293, p. 115732, 2022, ISSN: 0263-8223. DOI: <https://doi.org/10.1016/j.compstruct.2022.115732>.
- [5] F. Precision, *Why aluminum is essential in aerospace industry: A guide to applications and advantages*, Accessed: 2025-04-18, 2023. [Online]. Available: <https://flyingprecision.com/why-aluminum-is-essential-in-aerospace-industry-a-guide-to-applications-and-advantages/>.
- [6] Aeromorning, *Gkn aerospace leads development of ground-breaking hydrogen propulsion system for aircraft*, Accessed: 2025-03-31, 2021. [Online]. Available: <https://aeromorning.com/en/gkn-aerospace-leads-development-of-ground-breaking-hydrogen-propulsion-system-for-aircraft/#:~:text=GKN%20Aerospace%20leads%20development%20of%20ground-breaking%20hydrogen%20propulsion,forefront%20of%20next%20generation%20of%20sustainable%20aircraft%20technology>.
- [7] H. Li, X. Cao, Y. Liu *et al.*, “Safety of hydrogen storage and transportation: An overview on mechanisms, techniques, and challenges,” *Energy Reports*, vol. 8, pp. 6258–6269, 2022, ISSN: 2352-4847. DOI: <https://doi.org/10.1016/j.egyr.2022.04.067>.
- [8] L. W. McKeen, “1 - introduction to fatigue of plastics and elastomers,” in *Fatigue and Tribological Properties of Plastics and Elastomers (Third Edition)*, L. W. McKeen, Ed., Third Edition, William Andrew Publishing, 2016, pp. 1–26, ISBN: 978-0-323-44201-5. DOI: <https://doi.org/10.1016/B978-0-323-44201-5.00001-0>.
- [9] M. Sultan, A. Nassef, G. Abdulnaser and M. Saber, “A novel procedure to determine the hoop mechanical properties of pipe materials using ring elongation testing technique,” *International Journal of Pressure Vessels and Piping*, vol. 205, p. 105001, 2023, ISSN: 0308-0161. DOI: 10.1016/j.ijpvp.2023.105001.
- [10] A. J. Tomstad, S. Thomesen, T. Børvik and O. S. Hopperstad, “Effects of constituent particle content on ductile fracture in isotropic and anisotropic 6000-series aluminium alloys,” *Materials Science and Engineering: A*, vol. 820, p. 141420, 2021, ISSN: 0921-5093. DOI: 10.1016/j.msea.2021.141420.
- [11] S. Thomesen, O. S. Hopperstad and T. Børvik, “Anisotropic plasticity and fracture of three 6000-series aluminum alloys,” *Metals*, vol. 11, no. 4, p. 557, 2021. DOI: 10.3390/met11040557.
- [12] “Mechanics and full-field deformation study of the ring hoop tension test,” *International Journal of Solids and Structures*, vol. 51, no. 18, pp. 3042–3057, 2014, ISSN: 0020-7683. DOI: <https://doi.org/10.1016/j.ijsolstr.2014.04.023>.
- [13] A. International, *Astm e8/e8m-24: Standard test methods for tension testing of metallic materials*, Standard No. E8/E8M-24, ASTM International, 2024.
- [14] A. International, *Astm a370-22: Standard test methods and definitions for mechanical testing of steel products*, Accessed: 2025-04-08, 2022. [Online]. Available: <https://compass.astm.org/document/?contentCode=ASTM%7CA0370-22%7Cen-US>.
- [15] D. Kamerman, F. Cappia, K. Wheeler *et al.*, “Development of axial and ring hoop tension testing methods for nuclear fuel cladding tubes,” *Nuclear Materials and Energy*, vol. 31, p. 101175, 2022, ISSN: 2352-1791. DOI: 10.1016/j.nme.2022.101175.
- [16] J. Calaf-Chica, J. Martínez-Peña, P. M. B. Díez and M. P. Calzada, “Ring hoop tension test for yield strength estimation: Numerical analysis for a novel correlation method and applicability for mechanical testing of tubes and pipes,” *Mechanics of Materials*, vol. 169, p. 104295, 2022, ISSN: 0167-6636. DOI: 10.1016/j.mechmat.2022.104295.
- [17] J. Desquines, D. Koss, A. Motta, B. Cazalis and M. Petit, “The issue of stress state during mechanical tests to assess cladding performance during a reactivity-initiated accident (ria),” *Journal of Nuclear Materials*, vol. 412, no. 2, pp. 250–267, 2011, ISSN: 0022-3115. DOI: 10.1016/j.jnucmat.2011.03.015.
- [18] T. Kuwabara and F. Sugawara, “Multiaxial tube expansion test method for measurement of sheet metal deformation behavior under biaxial tension for a large strain range,” *International Journal of Plasticity*, vol. 45, pp. 103–118, 2013, ISSN: 0749-6419. DOI: 10.1016/j.ijplas.2012.12.003.
- [19] R. S. Hansen, D. W. Kamerman, P. G. Petersen and F. Cappia, “Evaluation of the ring tension test (rtt) for robust determination of material strengths,” *International Journal of Solids and Structures*, vol. 282, p. 112471, 2023, ISSN: 0020-7683. DOI: 10.1016/j.ijsolstr.2023.112471.

- [20] R. S. Daum, S. Majumdar, H. Tsai *et al.*, “Mechanical property testing of irradiated zircaloy cladding under reactor transient conditions,” *Small Specimen Test Techniques: Fourth Volume*, ASTM STP 1418, M. A. Sokolov, J. D. Landes and G. E. Lucas, Eds., 2002.
- [21] R. S. Hansen, D. W. Kamerman, P. G. Petersen and F. Cappia, “Mechanics of the ring tension test (rtt): A finite element-based investigation,” Idaho National Laboratory, Tech. Rep. INL/RPT-22-68606, Sep. 2022, Prepared for the U.S. Department of Energy Office of Nuclear Energy, under contract DE-AC07-05ID14517. [Online]. Available: https://inldigitallibrary.inl.gov/sites/STI/STI/Sort_63220.pdf.
- [22] A. Khalfallah, Z. Ktari, C. Leitão *et al.*, “New mandrel design for ring hoop tensile testing,” *Experimental Techniques*, vol. 45, pp. 769–787, 2021. DOI: 10.1007/s40799-021-00462-4.
- [23] B. Gurovich, A. Frolov and I. Fedotov, “Improved evaluation of ring tensile test ductility applied to neutron irradiated 42xnm tubes in the temperature range of (500–1100)°c,” *Nuclear Engineering and Technology*, vol. 52, no. 6, pp. 1213–1221, 2020, ISSN: 1738-5733. DOI: 10.1016/j.net.2019.11.019.
- [24] ASTM, *Astm e8/e8m - 24*, Accessed: 2025-01-15, 2024. [Online]. Available: <https://knowledge.bsigroup.com/products/standard-test-methods-for-tension-testing-of-metallic-materials-2>.
- [25] A. Genovese, G. A. D’Angelo, A. Sakhnevych and F. Farroni, “Review on friction and wear test rigs: An overview on the state of the art in tyre tread friction evaluation,” *Materials*, vol. 8, no. 9, p. 91, 2019. DOI: 10.3390/ma8090091.
- [26] W. Xu, X. Jin, Y. Zhang and X. Ren, “A study of effect of various normal force loading forms on friction-induced vibration,” *Advances in Mechanical Engineering*, vol. 10, no. 11, pp. 1–14, 2018. DOI: 10.1177/1687814018812750.
- [27] M. Lepicka, G. Górska, M. Grądzka-Dahlke and B. Ambrożkiewicz, “Analysis of tribological behaviour of titanium nitride-coated stainless steel using wavelet-based methods,” *Archive of Applied Mechanics*, vol. 91, no. 4, pp. 1501–1515, 2021. DOI: 10.1007/s00419-021-02016-x.
- [28] M. N. Helfrick, C. Niezrecki, P. Avitabile and T. Schmidt, “3d digital image correlation methods for full-field vibration measurement,” *Mechanical Systems and Signal Processing*, vol. 25, no. 3, pp. 917–927, 2011, ISSN: 0888-3270. DOI: 10.1016/j.ymssp.2010.08.013.
- [29] *BS 970: 1955 - Wrought steels for mechanical and allied engineering purposes*, London, UK, 1955.
- [30] The Aluminum Association, *Aluminum Standards and Data Metric SI*. Arlington, VA, USA: The Aluminum Association, 2017.
- [31] S. Davenport and R. Higginson, “Strain path effects under hot working: An introduction,” *Journal of Materials Processing Technology*, vol. 98, no. 3, pp. 267–291, 2000, ISSN: 0924-0136. DOI: [https://doi.org/10.1016/S0924-0136\(99\)00320-9](https://doi.org/10.1016/S0924-0136(99)00320-9).
- [32] C. L. Ali Khalfallah Zied Ktari and J. V. Fernandes, “New mandrel design for ring hoop tensile testing,” *Experimental Techniques*, vol. 45, no. 6, pp. 769–787, 2021. DOI: 10.1080/18811248.2007.9711560.
- [33] MatWeb, *Aluminum 6082-t6*, Accessed: 2025-04-08, 2001. [Online]. Available: <https://www.matweb.com/search/GetReference.aspx?matid=9432>.
- [34] L. Chang, S. Yuan, X. Huang and Z. Cai, “Determination of johnson-cook damage model for 7xxx laminated aluminum alloy and simulation application,” *Materials Today Communications*, vol. 34, p. 105224, 2023, ISSN: 2352-4928. DOI: 10.1016/j.mtcomm.2022.105224.